

RESEARCH ARTICLE

10.1029/2017JA024876

Special Section:

Atmospheric Gravity Wave Science in the Polar Regions and First Results from ANGIN

Key Points:

- A multiyear investigation of over 650 MSTIDs observed in the high latitudes, providing first full seasonal propagation characteristics
- This study provides novel statistical measurements of the vertical gravity wave spectrum in the lower thermosphere
- This study supports strong evidence for critical level and dissipative filtering of the gravity wave field with altitude

Correspondence to:

M. R. Negale,
Micheal.Negale@aggiemail.usu.edu

Citation:

Negale, M. R., Taylor, M. J., Nicolls, M. J., Vadas, S. L., Nielsen, K., & Heinselman, C. J. (2018). Seasonal propagation characteristics of MSTIDs observed at high latitudes over Central Alaska using the Poker Flat Incoherent Scatter Radar. *Journal of Geophysical Research: Space Physics*, 123, 5717–5737. <https://doi.org/10.1029/2017JA024876>

Received 12 OCT 2017

Accepted 12 MAY 2018

Accepted article online 21 MAY 2018

Published online 7 JUL 2018

Seasonal Propagation Characteristics of MSTIDs Observed at High Latitudes Over Central Alaska Using the Poker Flat Incoherent Scatter Radar

M. R. Negale¹ , M. J. Taylor¹ , M. J. Nicolls², S. L. Vadas³ , K. Nielsen⁴, and C. J. Heinselman⁵ 

¹Department of Physics and Center for Atmospheric and Space Sciences, Utah State University, Logan, UT, USA, ²Leo Labs, Menlo Park, CA, USA, ³Northwest Research Associates, Boulder, CO, USA, ⁴Department of Physics, Utah Valley University, Orem, UT, USA, ⁵EISCAT Scientific Association, Kiruna, Sweden

Abstract Near-continuous electron density measurements obtained over a ~3 year period, 2010–2013, using the Poker Flat Incoherent Scatter Radar (PFISR) in central Alaska (69°N, 147°W) have been analyzed to quantify the properties of over 650 high-latitude medium-scale traveling ionospheric disturbances (MSTIDs). Our analysis focused on the altitude range 100–300 km encompassing the lower ionosphere/thermosphere and yielded first full seasonal day/night distributions of MSTIDs at high northern latitudes with mean values: horizontal wavelength 446 km, horizontal phase speed 187 m/s, and period 41 min. These year-round measurements fill an important summertime gap in existing MSTID measurements revealing predominantly eastward wave propagation during the summer, while continued winter season observations agree well with previous reports of near southward propagating MSTIDs. Our 3 years of results suggest a cyclic change in the seasonal horizontal propagation directions that was found to be quantitatively consistent with critical level wind and dissipative filtering. Concurrent measurements of the vertical wavelength spectrum as a function of altitude also compared favorably in shape with that calculated using a theoretical dispersion relation (Vadas & Fritts, 2005, <https://doi.org/10.1029/2004JD005574>) for the thermosphere, but with a higher mean value. Evidence supporting the systematic broadening and shrinking in the azimuthal distributions of the MSTIDs during the course of the year was also found, as well as an unexpected correlation between the MSTID propagation directions and the AE index, both of which are under further investigation.

1. Introduction

Atmospheric gravity waves (GWs) are known to play important roles in the dynamics and thermal structure of the neutral upper atmosphere and ionosphere on a local, regional, and global scale. GWs from lower atmospheric sources grow in amplitude as they propagate into the upper atmosphere (assuming no significant dissipation), where they break and deposit energy and momentum, in spatially and temporally localized regions (e.g., Fritts & Alexander, 2003, and references therein). Studies in the mesosphere and lower thermosphere region (~80–110 km) show that GW dissipation leads to significant changes in the neutral atmosphere. Importantly, this process is responsible for the closure of the mesospheric jets, which leads to a strong mean meridional circulation that significantly cools the summer mesopause and warms the winter mesopause (e.g., Garcia & Solomon, 1985; Holton, 1982, 1983; Lindzen, 1981).

A broad range of wave observations and modeling studies have shown that those GWs generated in the lower atmosphere having large phase speeds can penetrate well into the thermosphere (e.g., Bauer, 1958; Bishop et al., 2006; Francis, 1973; Fritts & Vadas, 2008; Georges, 1968; Heale et al., 2014; Hocke & Tsuda, 2001; Hung & Smith, 1978; Kelley, 1997; Röttger, 1977; Vadas, 2007; Vadas & Liu, 2009; Vadas & Nicolls, 2008, 2009; Vadas et al., 2014; Waldock & Jones, 1987). Depending on their characteristics, these GWs may play important roles in both neutral thermosphere and plasma processes. For example, horizontal acceleration caused by GW momentum flux divergence from GW dissipation can result in substantial local forcing in the thermosphere, which significantly changes the neutral wind there (e.g., Vadas & Liu, 2013; Vadas & Nicolls, 2009; Vadas et al., 2014; Yigit & Medvedev, 2017). In addition, GWs capable of propagating to the bottom side of the F region (~150–300 km) may provide the seeds for the generation of equatorial spread F plasma bubbles (e.g., Huang & Kelley, 1996; Huang et al., 1993; Hysell et al., 1990; Sekar & Kelley, 1998; Sekar et al., 1995; Taylor et al., 1998).

As GWs propagate in the ionosphere region ($\sim 90\text{--}600$ km) they create periodic enhancements and depletions of the local ionospheric electron density, known as traveling ionospheric disturbances (TIDs; e.g., Hines, 1960; Hocke & Schlegel, 1996; Hooke, 1968; Hunsucker, 1982). TIDs have been studied since Munro (1948) first detected horizontal ionospheric motions using radio observations. Since these initial observations, the characteristics of TIDs have been investigated using a variety of techniques. These include (a) electron density measurements using vertical and oblique ionosondes (e.g., Afraimovich et al., 2008; Morgan et al., 1978; Ogawa et al., 2009; Tedd et al., 1984) and incoherent scatter radars (ISRs; e.g., Djuth et al., 1994, 1997; Fukao et al., 1993; Nicolls & Heinselman, 2007), (b) backscatter radar soundings (e.g., Bristow et al., 1994; Bristow & Greenwald, 1996; Frissell et al., 2014, 2016), (c) continuous wave (CW) Doppler measurements (e.g., Georges, 1967; Hung et al., 1979; Röttger, 1977), (d) total electron content (TEC) measurements using Global Positioning System (GPS) satellite constellations (e.g., Galushko et al., 2016; Nicolls et al., 2004; Onishi et al., 2009), and (e) optical airglow measurements (e.g., Kubota et al., 2011; Paulino et al., 2016; Shiokawa et al., 2003, 2009). All of these measurement techniques have their strengths and limitations. For example, the large networks of SuperDARN HF radars located at polar (and more recently midnorthern latitudes) initially designed to study the structure and dynamics of the high-latitude *F* region ionosphere (e.g., Chisham et al., 2007; Greenwald et al., 1995) also provide a powerful capability to remotely measure TID signatures in the *F* region ionosphere (e.g., Samson et al., 1990). However, these measurements are usually limited to winter daytime measurements when the *F* region density is sufficient to generate reflections (e.g., Bristow et al., 1994). Conversely, optical measurements using the thermospheric 630-nm airglow emission are restricted to nighttime measurements of the emission layer at $\sim 220\text{--}280$ km.

There are two main categories for TIDs: large-scale TIDs (LSTIDs) and medium-scale TIDs (MSTIDs) (e.g., Georges, 1968). LSTIDs can originate (1) in the high-latitude upper atmosphere generated mainly by Joule heating and auroral particle precipitation events (e.g., Chimonas & Hines, 1970; Richmond, 1978; Testud, 1970) and (2) in the thermosphere from horizontal body forces following the dissipation of GWs from deep convection (e.g., Vadas & Crowley, 2010; Vadas & Liu, 2009, 2013). LSTIDs exhibit periods in the range $\sim 0.5\text{--}3$ hr, horizontal wavelengths 1,000 km to several thousand kilometers, and phase speeds between 500 and 1,000 m/s (e.g., Hocke & Schlegel, 1996). In contrast, MSTIDs exhibit periods < 1 hr, horizontal wavelengths $\sim 100\text{--}1,000$ km, and typical phase speeds $\sim 250\text{--}400$ m/s (e.g., Ogawa et al., 1987; Samson et al., 1990). MSTIDs are a common occurrence in the thermosphere/*F* region ionosphere, and originate primarily from deep convection in the lower atmosphere (e.g., Crowley et al., 1987; Georges, 1968; Hocke & Schlegel, 1996; Ogawa et al., 1987; Waldock & Jones, 1986).

As an example, Pinger (1979) observed a single MSTID using the ISR at Chatanika, Alaska (65°N , 147°W ; currently operational at Sondrestrom, Greenland). The MSTID they investigated exhibited a period of ~ 37 min and propagated southward with a phase speed of ~ 208 m/s. They identified a filamentary auroral arc that was moving southward as a possible source for the MSTID. This said, there have been many other observations of MSTIDs suggesting tropospheric sources (e.g., Bishop et al., 2006; Davies & Baker, 1965; Davies & Jones, 1973; Frissell et al., 2016; Gossard, 1962; Hung & Kuo, 1978; Hung & Smith, 1978; Prasad et al., 1975). For example, Hung et al. (1979) observed MSTIDs using an HF Doppler sounder and determined that these MSTID events were associated with tornadoes via ray tracing and comparison with meteorology data. Waldock and Jones (1987) determined the characteristics of MSTIDs observed using the HF Doppler technique over Leicester, UK. Using reverse ray tracing through a modeled atmosphere, they determined that the source locations for these waves originated in the troposphere. They also found a moderate correlation between the occurrence frequency of MSTIDs and the intensity of the meteorological jet stream. Frissell et al. (2016) observed MSTIDs using an array of SuperDARN HF radars. They found a strong correlation between the occurrence of MSTIDs and the intensity of the stratospheric polar vortex.

While MSTIDs have been studied extensively in the high-latitude and mid-latitude *F* region, their global seasonal propagation characteristics are still not well known (e.g., Bristow & Greenwald, 1996; Bristow et al., 1994; Evans et al., 1983; Frissell et al., 2014; Grocott et al., 2013; Hernández-Pajares et al., 2012; Ishida et al., 2008; Kotake et al., 2007; Ogawa et al., 1987; Samson et al., 1989, 1990; Waldock & Jones, 1986). Table 1 lists results from several studies of MSTIDs at high latitudes where a large number of events have been measured, providing statistics on their propagation characteristics. Most of these studies determined the horizontal wavelength (λ_H), phase speed (c_H), observed period (τ), and direction of propagation (ϕ) of the wave, but often over a restricted altitude range in the thermosphere. To date, most MSTID studies have utilized multi-site radar systems such as the SuperDARN network and recently satellite observations of the TEC (e.g., Ding et al., 2011;

Table 1

MSTID Wave Parameter Results From Selected Studies at High Latitudes Illustrating the Broad Range of Wave Measurements

Location	Method	<i>N</i>	Date Range	Time	λ_H [km]	τ [min]	c_H [m/s]	ϕ [deg]	Reference
53.32°N, 49.39°N	SuperDARN	304	Nov 2012 to Apr 2015	Daytime	100–450	30–40	75–325	125–325° southward	Frissell et al. (2016)
52.16°N, 53.98°N			No summer data						
65.1°N	630 nm Airglow	44 nights	Nov 2001 to Apr 2002	Nighttime	100–400	20–60	80–200	210–270° southward	Kubota et al. (2011)
78°N	EISCAT	244	Mar 2007 to Feb 2008	Day and nighttime	—	30–120	~250	—	Vlasov et al. (2011)
~60°N	GPS TEC	—	2004–2011	Day and nighttime	50–350	13–27	150–250	90–270° southward	Hernández-Pajares et al. (2012)

Note. *N* is number of events.

Frissell et al., 2016; Galushko et al., 2016; Ishida et al., 2008). The results illustrate a broad range of wave parameters, although all lie within the MSTID category. The results consistently show that the observed waves almost always propagated southward during the winter times. However, there have been studies establishing the local time dependency of MSTIDs during the course of the day (e.g., Crowley et al., 1987; Fedorenko & Kryuchkov, 2013; Galushko et al., 2016; He et al., 2004; MacDougall et al., 2009).

This study focuses on MSTIDs at high latitudes using the Poker Flat Incoherent Scatter Radar (PFISR) operated at the Poker Flat Research Range (65.13°N, 147.47°W, MLAT = 65.4°N) near Fairbanks, Alaska. PFISR is a part of the Advanced Modular Incoherent Scatter Radar class of ISRs, and has the capability to rapidly observe different regions of the ionosphere using pulse-to-pulse beam steering. This makes PFISR an ideal instrument for investigating the three-dimensional properties of TIDs at high latitudes (e.g., Nicolls & Heinselman, 2007; Vadas & Nicolls, 2008, 2009; Waldock & Jones, 1986). Nicolls and Heinselman (2007) made observations of a single MSTID event that occurred on 13 December 2006. In their study, they used the (then) recently developed phased array PFISR to make novel multibeam (10 beams used) measurements of an MSTID. Their observations provided measurements of the MSTID over an extended altitude range ~160–220 km. The wave event lasted for ~1.5 hr and exhibited height-integrated horizontal wavelength of ~187 km, horizontal phase speed of ~140 m/s, observed period of ~22 min, southeastward (~150°) propagation direction, and vertical wavelength of ~231 km.

Using the data obtained from PFISR, over 650 MSTIDs were detected and measured over an extended period from August 2010 to April 2013, enabling a comprehensive study of their seasonal characteristics. To our knowledge, this study provides the most extensive height-resolved investigation of MSTIDs to date. MSTID detection and selection is described in the analysis section using a single MSTID event observed on 18 May 2011. Using previously developed, well-proven methods of spatially separated ionospheric measurements (e.g., Afraimovich et al., 1999; Bristow & Greenwald, 1996; Nicolls & Heinselman, 2007; Reid, 1986), we were able to determine the period and horizontal wave vector as a function of altitude for this MSTID event and determine the vertical wavelength and altitudinal structure. This analysis is followed by a discussion of our results, which includes a new investigation into the seasonal characteristics of the propagation directions, comparisons with published SuperDARN measurements, and new observations of the vertical wavelength spectra. Finally, the discussion includes consideration of the effects of critical level and dissipative filtering on the MSTIDs.

2. Instrumentation

Figure 1 shows the location of PFISR in central Alaska. PFISR is capable of measuring 473 preprogrammed look directions within the grating lobe limits, as indicated in Figure 1. The individual beam positions are selectable as determined by the type of ionospheric observations to be investigated. The insert shows the latitudinal and longitudinal ranges (in km), with the vertical axis pointing northward and the horizontal axis pointing eastward, of the grating lobe limit plotted at 300 km altitude. The four-beam configuration used primarily for this study is indicated by the black dots.

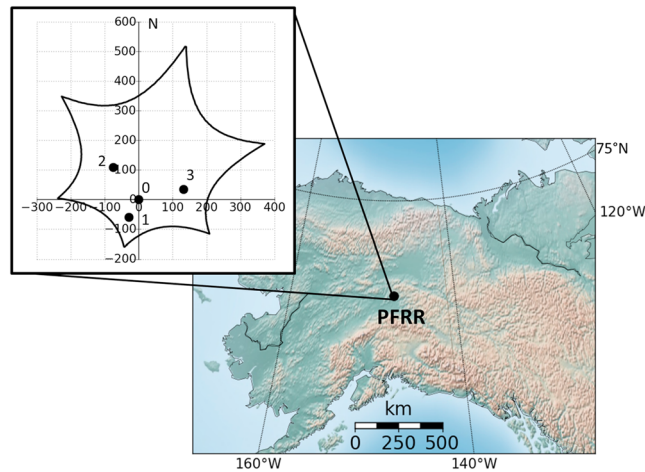


Figure 1. Map showing location of PFISR in central Alaska (labeled PFRR) and the latitudinal and longitudinal extent of the PFISR observations mapped at 300 km altitude. PFRR = Poker Flat Research Range; PFISR = Poker Flat Incoherent Scatter Radar.

The four-beam configuration we use here was introduced for the International Polar Year (IPY) that began on 1 March 2007. The primary goal of IPY was to obtain high-quality ionospheric data with good spatial coverage on a near continuous basis and was run when no other special programs were in operation (e.g., Sojka et al., 2009). This mode was also operated at lower power, which resulted in a maximum working altitude range of ~ 300 – 500 km, depending on the ionospheric conditions. The four-beam configuration was composed of a zenith-pointing beam (elevation (el) = 90° , azimuth (az) = 14°), a beam pointing up the magnetic field line (el = 78° , az = -154°), and two off-zenith beams to the north-northwest (NNW; el = 66° , az = -35°) and to the east-northeast (ENE; el = 66° , az = 75°), as shown in Figure 1 insert. The IPY mode consists of a $480\text{-}\mu\text{s}$ long pulse designed for F region studies (e.g., Sojka et al., 2009) and integrated data were obtained from the Madrigal database (<http://www.openmadrigal.org>) available at 5-min intervals. While this four-beam configuration is less than those employed by Nicolls and Heinselman (2007) in their earlier MSTID study using PFISR, this configuration provides the necessary zenith and spatial sampling needed to clearly resolve the three-dimensional wave vectors (as described in section 3.2; e.g., Nicolls & Heinselman, 2007; Vadas & Nicolls, 2009; Waldock & Jones, 1986).

PFISR was operated near-continuously over a ~ 32 -month period from August 2010 to April 2013, thereby obtaining 428 days of observations. From August 2010 to December 2011, most of the data were obtained using the IPY mode; over $\sim 75\%$ of the MSTIDs reported in this investigation were measured using this four-beam configuration. From January 2012 to April 2013, IPY measurements were also made, but less frequently because of other program operations not suitable for our study.

3. Analysis

3.1. MSTID Identification and Localization

Our analysis is based on the *case study* method employed by Nicolls and Heinselman (2007) who used PFISR in a 10-beam mode, but adapted to the four-beam IPY mode. It also includes additional checks to ensure clear MSTID identification within this large data set. We illustrate our analysis method with a well-defined MSTID observed on 18 May 2011. Electron densities were measured by each beam as a function of time and range. Figure 2a shows the electron density profile for the vertically pointing beam for this event. Close visual inspection of these data reveal clear evidence of a vertically extensive, periodic ionospheric perturbation. This high-frequency event was observed from ~ 11 to 18 UT and was coherent over the altitude range of ~ 100 – 350 km, as indicated by the dashed area in Figure 2a. Also note that around ~ 100 – 200 km from 10 to 12 UT, there is a depleted electron density region associated with auroral upwelling, which can limit the ability to make accurate nighttime MSTID measurements.

To investigate this event, we filter the electron density perturbations, as shown in Figure 2b. The relative electron density perturbations are then calculated via

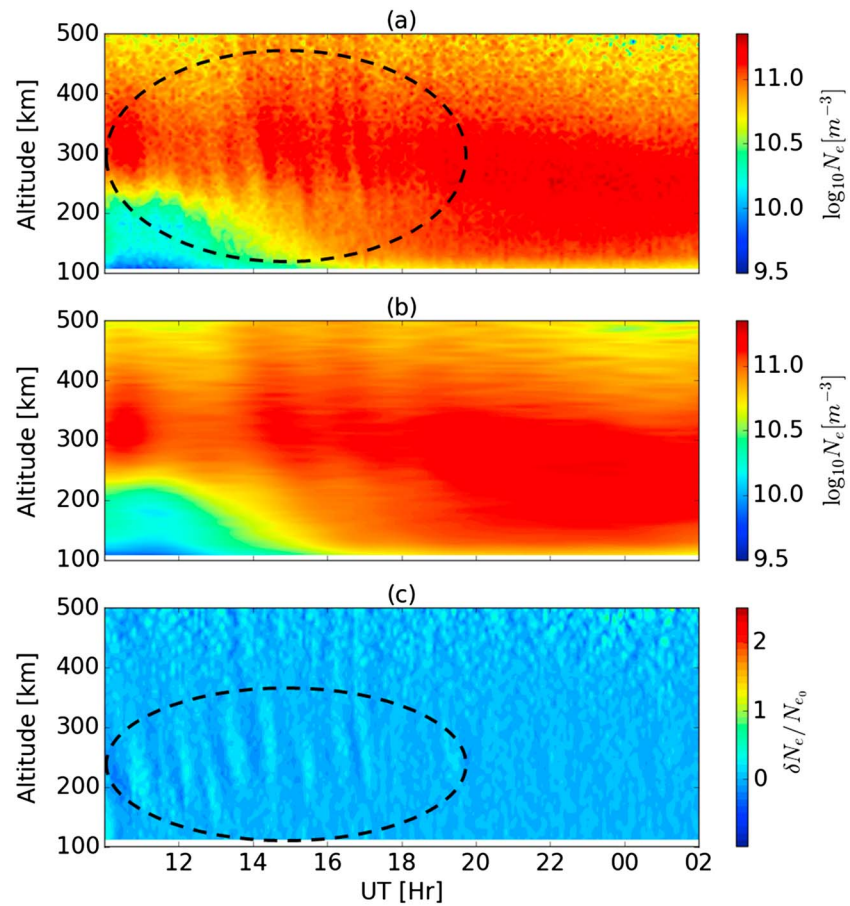


Figure 2. Illustration of the analysis procedure on 18 May 2011 at PFISR. (a) Measured electron densities from the vertically pointing beam. (b) Background electron densities estimated using a low-pass filter. (c) Derived relative electron density perturbations. PFISR = Poker Flat Incoherent Scatter Radar.

$$\frac{\delta N_e}{N_{e_0}} = \frac{N_e - N_{e_0}}{N_{e_0}}, \quad (1)$$

where N_e is the measured electron density and N_{e_0} is the filtered electron density. Figure 2c shows the relative electron density perturbations for this event. High-frequency waves are clearly seen up to ~300–350 km.

Due to the large amounts of data, we have developed a method to detect and isolate the occurrence and periodicities of a broad range of MSTIDs in the data set. This involves constructing spectrograms of the data for every PFISR run utilizing an uncorrected long-pulse measurement (~5-km altitude resolution). This procedure was performed for each beam in each individual experiment. Figure 3 shows a spectrogram for the zenith-pointing beam using our example event (from Figure 2). Each spectrogram is constructed by taking a subset (i.e., window) in altitude (in 25-km steps, thus containing 5-km altitudes) and in time (120-min intervals) of the derived relative electron density perturbations. This procedure is typically performed over the altitude range 100–500 km. The altitude bin over which we average is a selectable parameter, and bin widths of 25 km were chosen to capture the spectral information used to identify the event and at the same time provide good determination of the altitude extent of each event. For each resolved altitude in the window, a Lomb Scargle (LS) spectral analysis is performed. The resultant LS powers are then averaged to yield a single-power spectrum for that window and are assigned a time stamp corresponding to the center of the time interval. The window is then incremented by 20 min and the process is repeated until the time series ends. This analysis is then repeated for the subsequent altitude bins, resulting in the spectrogram shown in Figure 3. Vertically extensive, quasi-coherent wave events are then identified visually from the spectrogram via choosing events with discrete frequency signatures that exist in multiple consecutive altitude bins having similar durations. Our example MSTID event (from Figure 2) is clearly seen extending in altitude from 175 to 350 km and from

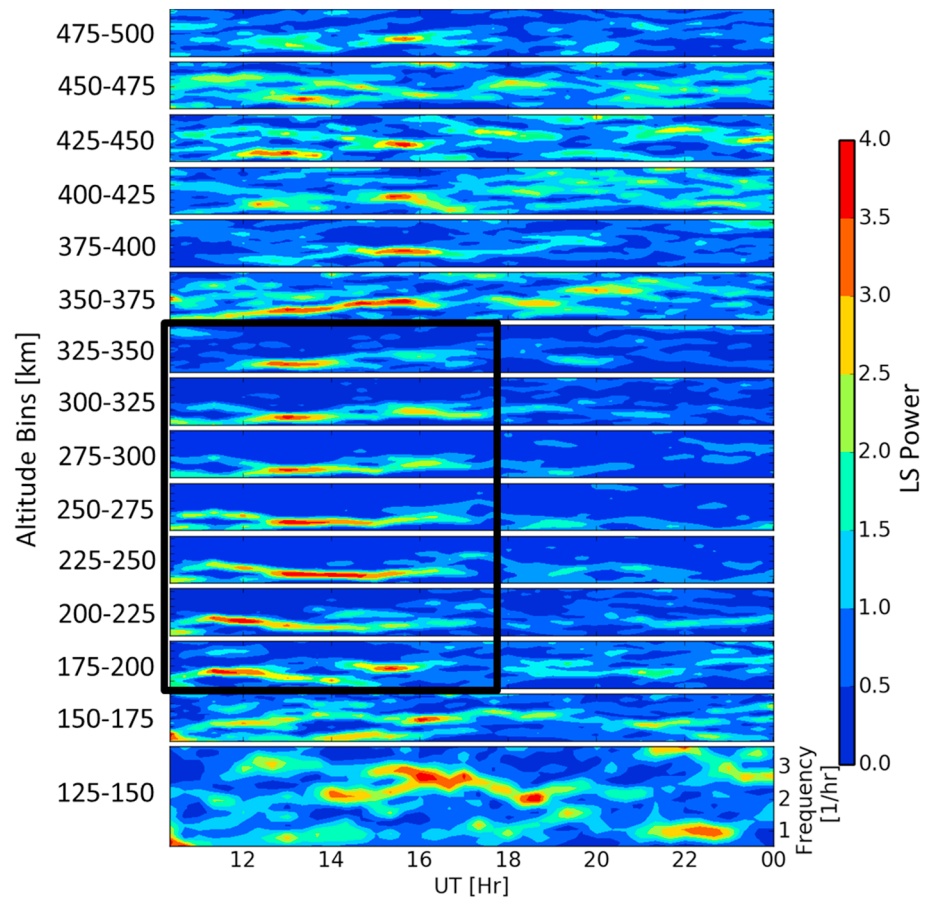


Figure 3. Spectrograms of the case shown on 18 May 2011 for the zenith-pointing beam in altitude bins of 25 km from 125 to 500-km altitude and 10–24 UT. The box identifies the medium-scale traveling ionospheric disturbance event.

~10 to 18 UT in Figure 3. In addition to identifying MSTID events, the spectrograms are also used to estimate the dominant periodicity of the event (in this case, ~55 min).

Once an MSTID event is identified in a specific altitude range and duration, the relative electron density perturbations for all of the beams are limited to this same altitude range and duration. Figure 4a shows the derived relative electron density perturbations for the MSTID event described above for the zenith-pointing beam. The constant phase lines of the MSTID slope downward in time, indicative of upward energy propagation for GWs; this is consistent with a lower atmospheric GW source. Finally, the relative electron densities are band-passed filtered to further enhance the phase structures (Figure 4b), as previously employed by Nicolls and Heinselman (2007). For each event, the filter is centered on the dominant period of the MSTID. The filter bandwidth is chosen to contain the dominant wave periods present in the spectrogram. The cutoff periods of the bandpass filter are the same for all beams and at all altitudes for a particular event. For example, the dominant period of the 18 May 2011 event in Figure 3 is ~55 min with a lower cutoff period of 40 min and an upper cutoff period of 85 min encompassing the dominant peaks selected by combining the altitude-binned spectrograms into a single spectrogram. Each event has its own selected bandwidth. This technique is successful in identifying MSTIDs in the thermosphere/ionosphere, and closely follows previously published methods (e.g., Vadas & Nicolls, 2008). Note that the spectrogram method was first referenced in Georges (1968) and utilized by Nicolls et al. (2014) to identify GWs at the Arecibo Observatory.

3.2. Determination of MSTID Parameters

The wave analysis we use here is well developed and has been employed in several prior studies (e.g., Nicolls & Heinselman, 2007; Reid, 1986; Waldoock & Jones, 1986). For each beam the electron density perturbations at each altitude are used to calculate the LS power spectrum and data with peak powers exceeding a >95% confidence level are subsequently used. For the IPY data, we then use the following beam pairs: (2,3), (1,3),

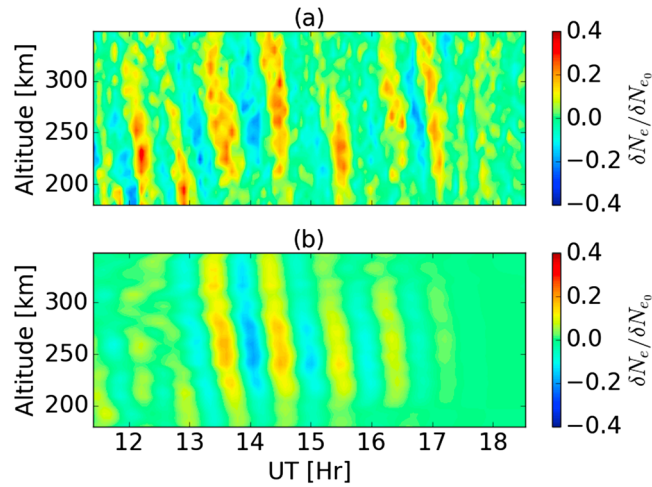


Figure 4. (a) Derived relative electron density perturbations and (b) band-passed perturbations used in the medium-scale traveling ionospheric disturbance analysis for the case on 18 May 2011 for the zenith-pointing beam.

(1,0), (0,3) for analysis. If the dominant periods from each beam in a beam pair differed by more than 10 min, then data from this beam pair at this altitude are also not used. These selection criteria have proved necessary to effectively identify dominant periodicities as a function of altitude. We perform this procedure automatically for all altitudes and for each beam pair.

The selected data are then used to calculate the complex cross-spectra using relative electron density perturbations from each beam pair. We then compare the peak period of the spectrum with the dominant periods of each beam separately. If these two periods differed by more than 10 min, then this beam pair was also not used. This procedure was repeated for each beam pair to create a final data set.

In the process of obtaining the dominant period (τ) from the cross-spectrum, the phase delay (y) is also obtained. We then utilize the phase delays as a function of altitude to perform a selection test; in particular, we require the phase delay between two beams to be consistent (see Figure 5). This is because the phase delay relates to the time (δt) that the MSTID takes to propagate from one beam to the other, and to the dominant period of the wave (e.g., Nicolls & Heinselman, 2007):

$$y_{ij} = \frac{2\pi \delta t_{ij}}{\tau}, \quad (2)$$

where y_{ij} is the phase delay between beams i and j . Errors in the phase delays are estimated by the full width at half maximum of the complex cross-spectrum, as shown in Figure 5, centered on the dominant wave period. It is important to note that this estimate includes both errors due to statistical errors and, possibly, the influence of nondominant periods. For a measurement to be considered successful, at least two beam pairs must have

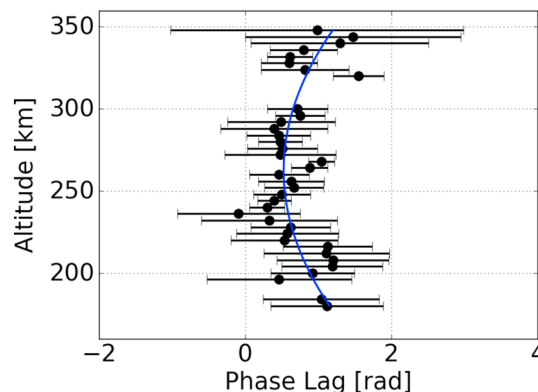


Figure 5. Phase delays as a function of altitude (175–350 km) using correlations with beams 1 and 0 for the case on 18 May 2011. The solid line shows a second-order polynomial least squares fit to the data.

valid data at each altitude. This resultant data set is then used to compute the wave parameters as a function of altitude, as described below.

We calculate the vector (\vec{A}), which points from one beam measurement to the other, using the measurement azimuth, elevation, and range. This vector is the component of the wave vector (\vec{k}) that can be estimated from these two beams. For a known \vec{k} , the forward problem (calculating what the measurement would be) then becomes

$$\vec{A} \cdot \vec{k} = \vec{y} + \delta\vec{y}. \quad (3)$$

Here we have also included the measurement error into the model. For more than two valid beam pairs, then we can estimate the wave vector using a weighted linear least squares estimate:

$$\vec{k} = (A^T C^{-1} A)^{-1} A^T C^{-1} \vec{y}. \quad (4)$$

The choice of a weighting matrix C would, in an ideal case, be the variance-covariance matrix for the measurements, thus yielding a Best Linear Unbiased Estimator (BLUE) for \vec{k} . As mentioned earlier, however, the errors are not purely statistical, though they will include the effects of electron density estimation errors which are then reflected in the phase errors from the cross-spectra. This contribution to the variance-covariance matrix would result in off-diagonal terms because errors in, for example, densities in direction 0 would impact phases for both of the pairs (0,1) and (0,3). Unfortunately, the error covariances are not readily available in the data sets (recall that the variances are obtained via cross-spectral widths) and, though potentially suboptimal, we use the following for the weighting matrix:

$$C = \begin{bmatrix} (\delta y_1)^2 & \dots & 0 \\ \vdots & (\delta y_2)^2 & \vdots \\ 0 & \dots & (\delta y_n)^2 \end{bmatrix}, \quad (5)$$

(e.g., Heinselman & Nicolls, 2008). This method allows us to estimate the errors in the wave numbers. Figure 5 shows the phase delays from correlations between the zenith-pointing beam and the off-zenith beam (beams 0 and 1) over the altitude range 175–350 km, where the signal was strongest. Again, we use the example event on 18 May 2011 to illustrate the analysis method. The solid line shows the least squares fit to the data to better illustrate how the phase delays change with altitude and was not applied in the analysis. These results are typical of our analysis, and show phase delays that change with altitude in a consistent manner, within the limits of the measurements.

Note, computer simulations were constructed by taking a model ionosphere using IRI and added perturbations of the form $\delta N_e(\vec{r}, t) = A \cos(\vec{k} \cdot \vec{r} - \omega t) + \text{noise}$, (where A is the amplitude, \vec{r} is the position measurement), and inputting various parameters for \vec{k} and ω . These simulations successfully reproduced original input parameters (not shown) for the range of parameters presented in the paper. This suggests that our approximation for the variance-covariance matrix does not seriously degrade our results.

4. Results

4.1. MSTID Event Characteristics

The results for the analysis of the 18 May 2011 event yield the observed periods (Figure 6a) and the horizontal wave vector as functions of altitude. The horizontal wavelength (Figure 6b) is then calculated from the horizontal wave numbers ($\lambda_H = 2\pi / \sqrt{k_x^2 + k_y^2}$). The phase speeds (Figure 6c) are derived using the observed period and the horizontal wavelength ($c_H = \lambda_H / \tau$). The direction of propagation is determined from the horizontal wave vector ($\phi = \tan^{-1}(k_y/k_x)$), shown in Figure 6d in degrees clockwise from north (i.e., azimuth). Note that the full wave vector (i.e., including the vertical wave number) is not determined at this stage because correlations between adjacent beams are performed at similar altitudes for comparison with SuperDARN results (section 6.2). The vertical wavelengths are presented in section 6.4.

For this event, the wave period increases from ~55 min at 175 km to ~60 min at 300-km altitude, with an altitude-averaged value of 57 ± 1 min, where the error corresponds to the standard deviation of the mean. The horizontal wavelength also increases from ~260 km to ~400 km over the measured altitude range, with an altitude average of 372 ± 18 km. The derived phase speeds increase from ~80 m/s to ~110 m/s, with a mean of 108 ± 5 m/s. The direction of propagation changed with altitude from ~10° to ~50° at 300-km altitude,

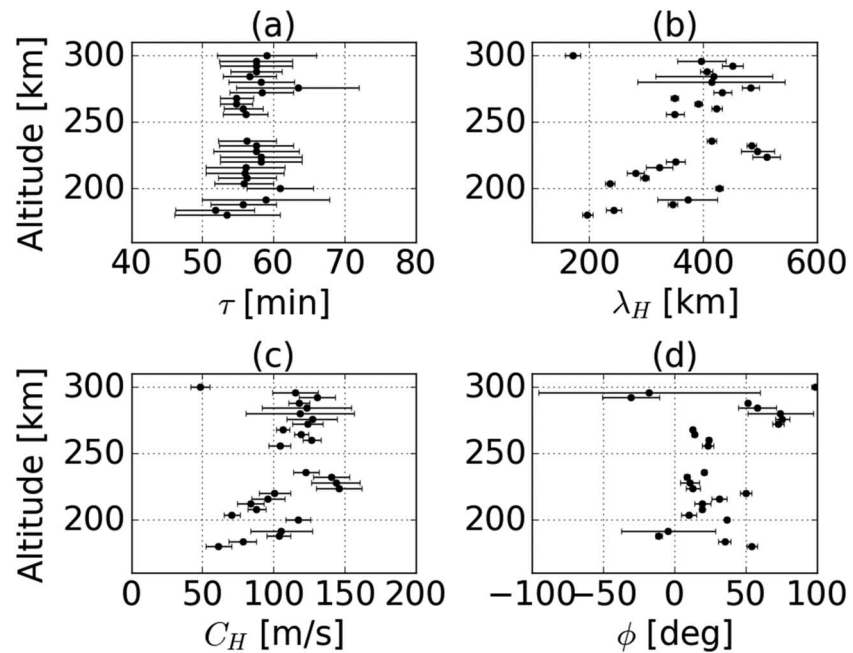


Figure 6. Derived (a) period, (b) horizontal wavelength, (c) horizontal phase speed, and (d) propagation direction as a function of altitude for the 18 May 2011 event. The error bars represent the derived uncertainties for the individual wave measurements as a function of altitude.

with a mean of 29° . Note, for analysis purposes we only selected wave events that exhibited consistency with altitude as illustrated in Figure 6d. Taking the height-averaged value is one simple way of representing their properties for comparison with other data sets, such as SuperDARN (e.g., Frisell et al., 2014, 2016; Ishida et al., 2008), as well as in our seasonal analyses (section 6.1).

4.2. MSTID Statistical Characteristics

Using the analysis methods described above, 652 MSTID events have been identified from August 2010 to April 2013. The observed MSTID events range from 100 to 450 km in altitude. However, because of the reduced signal at higher altitudes, and in order to better compare our statistical results with published measurements, we limit the data products presented here to an altitude range of 100–300 km. Figure 7d shows a summary of the mean altitude where each MSTID event occurred. For example, if an event occurred over the altitude range of 100–300 km, then the mean altitude for that event was 200 km. Figures 7a–7c show the frequency distributions for the altitude-averaged horizontal wave parameters. The periods exhibit an interquartile range (25th–75th percentile) from ~ 37 to 44 min, horizontal wavelengths from ~ 369 to 514 km, and phase speeds from ~ 155 to 212 m/s. Mean values, medians, and interquartile ranges are summarized in Table 2. These results compare exceptionally well with other MSTID studies at high, middle, and low latitudes (e.g., Bristow et al., 1994; Bristow & Greenwald, 1996; Evans et al., 1983; Frisell et al., 2014, 2016; Grocott et al., 2013; Hernández-Pajares et al., 2012; Ishida et al., 2008; Kotake et al., 2007; Ogawa et al., 1987; Samson et al., 1989, 1990; Waldock & Jones, 1986). However, our data also enable an investigation into the variability with altitude and the seasonal changes of the wave parameters.

Figure 7e shows the height-averaged phase velocity distribution of 651 MSTID events. For illustrative purposes the maximum phase speed is limited to 400 m/s. The predominant propagation direction of MSTID is

Table 2
Mean Values, Medians, and Interquartile Range (Defined From the 25th–75th Percentile)

Parameter	Mean	Median	Range
λ_H [km]	446	431	369–514
τ [min]	41	41	37–44
C_H [m/s]	187	181	155–212
ϕ [deg]	120	120	84–160

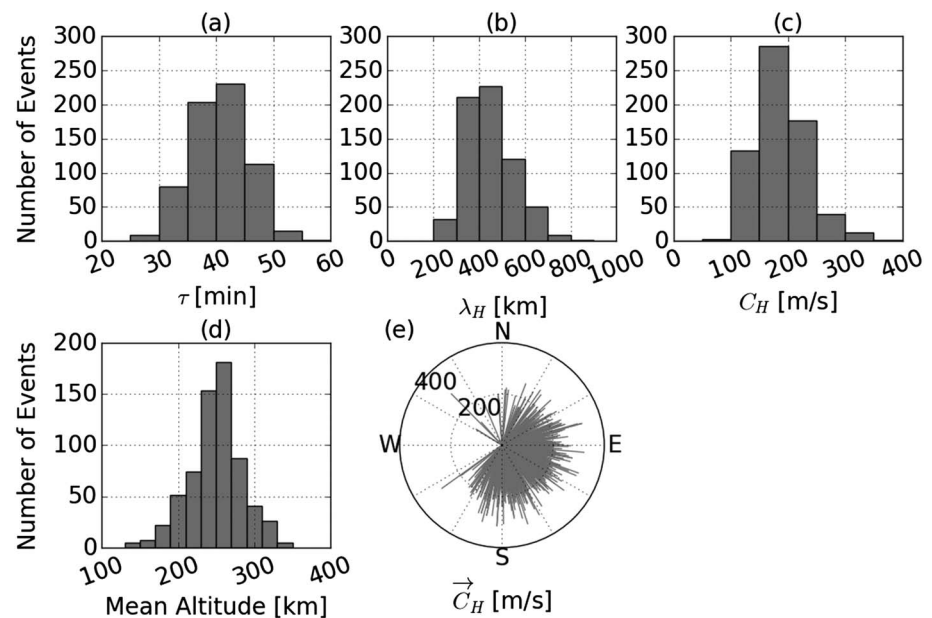


Figure 7. (a)–(c) Frequency distributions for the observed horizontal wave parameters. (d) Distribution of the mean altitude of each observation (~68% of events occurred with mean altitude $\bar{z} \leq 250$ km). (e) Horizontal phase velocities.

southeast, but extends from north through the southwest directions. Remarkably very few (<5%) of the waves were detected propagating westward over the broad 120° azimuth range 240–360°. Note also that one very high phase speed event (not shown here) exhibited a phase speed of ~500 m/s (azimuth 112°), which is close to the speed of sound in the thermosphere. In comparison, the smallest observed phase speed was ~86 m/s. In total, 97% of the observed MSTIDs exhibit phase speeds between 100 and 300 m/s (mean value 187 m/s, see Table 2).

5. Altitudinal Variability

We now investigate the variability of the wave parameters with altitude. Figure 8 shows the median of the wave parameters in 50-km-altitude bins from 100 to 300 km, where error bars represent the interquartile range. Of key importance is that the wave periods and azimuths are nearly constant with altitude, while both the horizontal wavelengths and the phase speeds increase systematically with altitude (i.e., ~20% increase for both the wavelengths and the phase speeds).

To date there have been very few reports showing the variability of MSTID parameters with altitude at high latitudes. These investigations mainly used ISR and ionosonde techniques, but with limited data and only one study at high latitudes using the EISCAT radar (e.g., Djuth et al., 1997; Ma et al., 1998; Nicolls et al., 2014; Oliver et al., 1997; Ratovsky et al., 2008; Tedd et al., 1984; Vadas, 2007). In particular Nicolls et al. (2014) reported TID height structure from Arecibo Observatory (18°N) obtained on two consecutive days (23–25 July 2009). Their Figure 13, plotted over the same altitude range as our results (100–300 km), shows that both the horizontal wavelength and phase speed increase with altitude, while the wave periods remained essentially constant with altitude. Our much larger ensemble of high-latitude MSTIDs agree very well the more limited events by Nicolls et al. (2014). Along with our new measurements, these studies show that the wave parameters change with altitude in the thermosphere.

6. Discussion

In this paper we used data obtained from PFISR from August 2010 to April 2013 to obtain new results on the statistical characteristics of high-latitude MSTIDs and their vertical variability. We now discuss the seasonal characteristics and compare our results with those in the literature. This is followed by an investigation of critical level and dissipative filtering effects on the propagation spectrum. We include a novel investigation of the vertical wavelength spectrum.

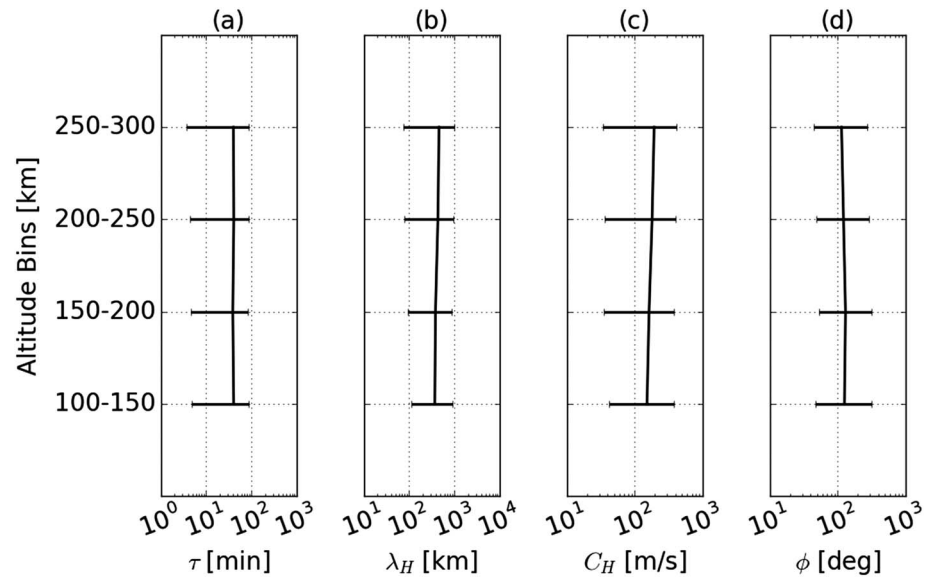


Figure 8. Medians of the (a) periods, (b) horizontal wavelengths, (c) horizontal phase speeds, and (d) propagation directions in 50-km-altitude bins showing how they change with altitude with error bars representing the interquartile ranges.

6.1. MSTID Seasonal Variability

Figures 9a–9d plots the wave parameters (τ , λ_H , c_H , ϕ) for each MSTID event (gray dots) as a function of time for the duration of this 32 month study as well as the mean altitude (Figure 9e) for each event. All plots utilize the same time scale to facilitate comparison. Note the reduction in number of measurements after January 2012 when fewer IPY measurements were conducted, as noted in section 2. The observed wave periods (Figure 9a) vary little over the course of this 32 month study with a majority of events within 30–60 min. The horizontal wavelengths (Figure 9b) and phase speeds (Figure 9c) also exhibited no significant variation in their mean values during this extended period. However, the directions of propagations appear to exhibit systematic variability with time, as indicated in Figure 9d. During the months September 2010 to February 2011, the MSTIDs are seen to propagate more southward and then go back to eastward propagation during the months March 2011 to September 2011. The directions of propagation increase again during the months September 2011 to April 2012, suggesting a cyclic behavior.

To further investigate the seasonal variability of the MSTID propagation directions during the approximately nine consecutive seasons of observations, we sum the data into three seasons: summer, winter, and equinox (spring + fall), each comprising four months of the year. Figure 10 shows polar plots with the results for the three winter seasons (November to February), three summer seasons (May to August), and three equinox periods (March to April and September to October). The results reveal striking seasonal changes in the dominant wave propagation direction. The MSTIDs observed during the winter months (Figure 10a) propagated predominantly southward, with 45% of the waves propagating within $\pm 30^\circ$ of 165° azimuth. In contrast, during the summer months (Figure 10c) the waves exhibit a strong preference for eastward propagation, with $\sim 50\%$ of the waves propagating within $\pm 30^\circ$ of due east. The spring and fall equinox periods (Figure 10b) yield similar results to each other, with the waves mainly propagating southeastward, with 45% propagating within $\pm 30^\circ$ of 120° azimuth. This figure further demonstrates the sparseness of MSTIDs propagating in the southwest through northwest quadrants (also see Figure 7e). Importantly, our full seasonal measurements suggest a consistent cyclic picture with eastward propagation during the summer months, transitioning to southeastward during the equinox periods and then to predominantly southward during the winter seasons. Thereafter, the cycle continues by transitioning back to southeastward during the spring and returning to eastward during the summer.

6.2. Comparisons With Other Results

Our findings obtained over several seasons, indicate strong seasonal variability in the MSTID propagation directions at this high-latitude location. Although there are several previous climatological studies of MSTIDs at middle and low latitudes (e.g., Crowley et al., 1987; Ding et al., 2011; Frissell et al., 2014; Ishida et al.,

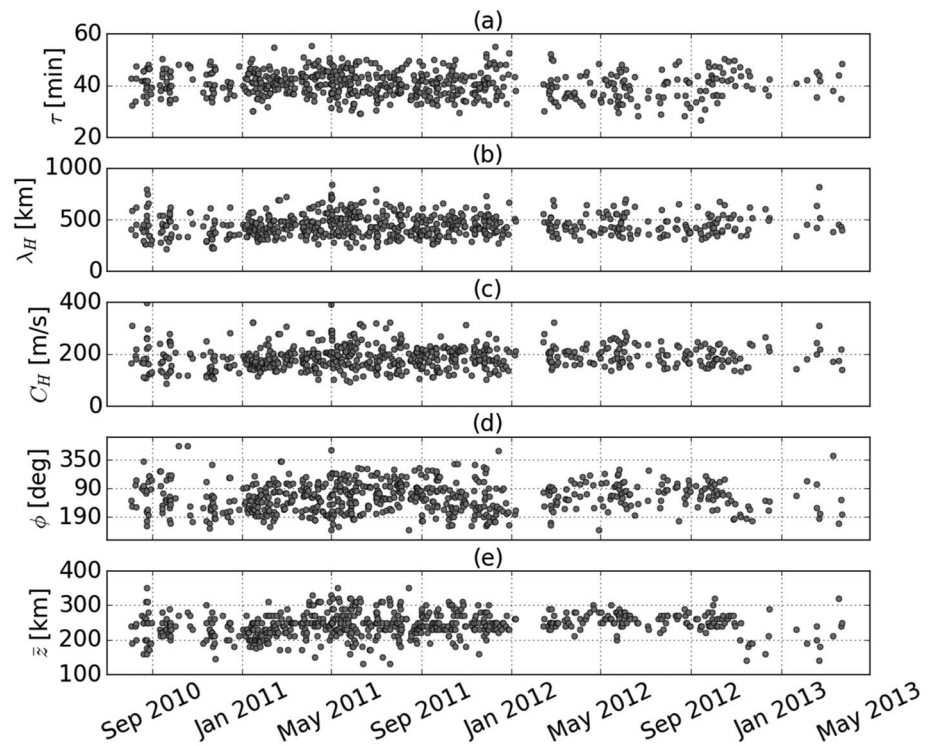


Figure 9. (a)–(d) Measured wave parameters as a function of time over the 32-month duration of this study. Each dot represents a single medium-scale traveling ionospheric disturbance event. Azimuthal directions are plotted clockwise from north. (e) Shows the mean altitude of each Poker Flat Incoherent Scatter Radar experiment (gray dot).

2008; Kubota et al., 2011), seasonal measurements at high latitudes are sparse and their properties are not well known.

Hernández-Pajares et al. (2012) reported a long-term climatology study of MSTIDs observed using TEC measurements at high, middle, and low latitudes. For their high northern latitude study, they used data from 13 GPS receivers located in southern Alaska recorded from 2004 to 2011 (see Table 1). In their seasonal study of the phase velocities, they determined that the fall and winter propagation directions are mainly south-eastward. Their data are presented in scatter plots and indicate many events during the winter season, which our results agree with (Figures 10a and 10b). In contrast, their summer time scatter plots are sparse and indicate MSTIDs propagating toward the northwest and the southeast, in contrast to our measurements of strong eastward propagation. This may be because the primary contributions to the TEC measurements are at the *F* peak, which is at much higher altitudes than our measurements here.

The SuperDARN network of HF radars has provided extensive high-latitude studies, enabling a quantitative comparison with our PFISR results. SuperDARN radars use the ground scatter technique to image MSTIDs

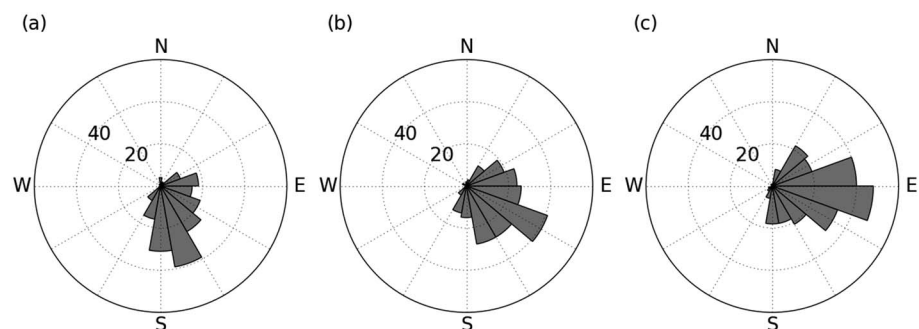


Figure 10. Propagation direction distributions for (a) winter (with 192 MSTID events), (b) equinoxes (with 219 MSTID events), and (c) summer (with 241 MSTID events). MSTID = medium-scale traveling ionospheric disturbances.

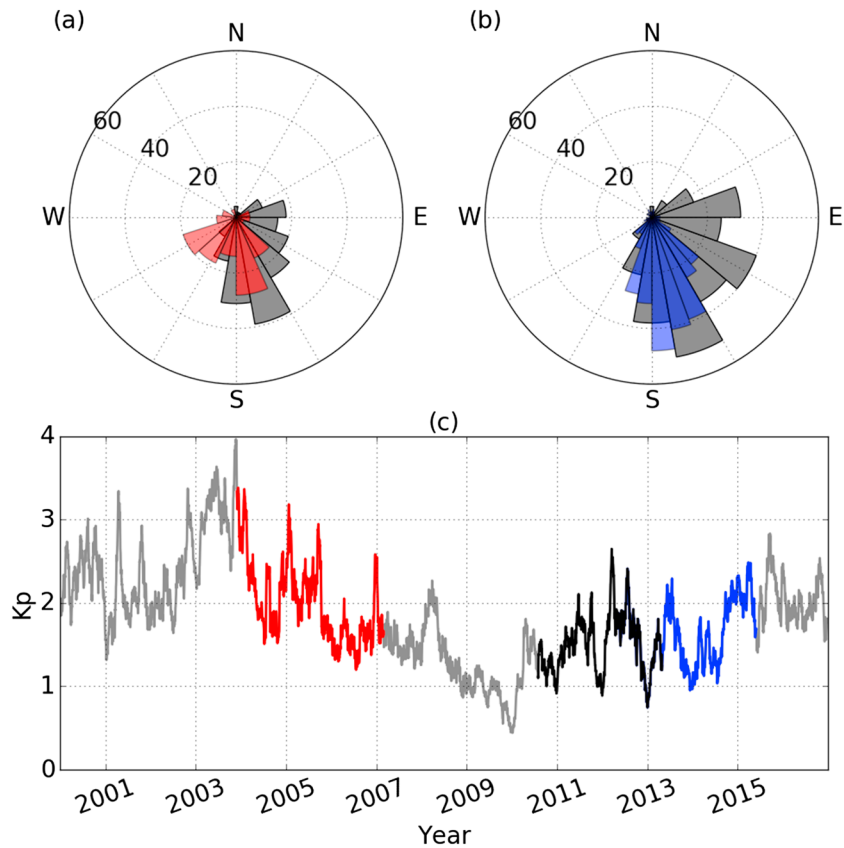


Figure 11. (a) Comparison of propagation directions with Ishida et al., 2008 (2008, red bars; auroral region measurements; 2003–2007) and PFISR (gray bars). (b) Comparison of the propagation directions with Frissell et al., 2016 (2016, blue bars; high-latitude measurements; May 2012 to May 2015) and PFISR (gray bars). (c) Kp (gray line). The overlaid red line is the date range for Ishida et al. (2008), the overlaid blue line is the date range for Frissell et al. (2016), and the overlaid black line is the date range for this PFISR study. PFISR = Poker Flat Incoherent Scatter Radar.

when ionospheric conditions enable observations of the *F* region (e.g., Bristow et al., 1994). This condition occurs primarily during daylight hours in the fall and winter months. We will now compare the propagation directions of the observed MSTIDs with those reported by Ishida et al. (2008) and Frissell et al. (2016).

The study by Ishida et al. (2008) reported 15 months of data during the fall and winter (December 2003 to February 2007) from the Kodiak and King Salmon radars in southern Alaska (see Table 1 for details). This allows for a direct comparison with our TID results for the winter/fall period. Their Figure 3a summarizes the results over three consecutive winter seasons comprising 134 MSTID events. We see that our observed wave parameters are very similar to their results (see Table 1 for comparison). Importantly, Ishida et al. (2008) also found that the winter time propagation directions were strongly southward, with a noticeable southwestward component.

To illustrate the high correlation with our results, Figure 11a overlays the azimuthal propagation distributions from Ishida et al. (2008) (red) with this PFISR study (gray) for the winter period (November to February). The data compare very favorably. It is interesting to note that Ishida et al. (2008) also show very little northward waves. Since the Ishida et al. (2008) results span a period of 10 years, Figure 11a strongly suggests that the climatology for high-latitude MSTIDs is reasonably stable during the winter at this geographical location. Figure 11c shows the monthly averaged Kp indices (obtained from NASA's OMNIWeb) during this 10-year period. The Ishida et al. (2008) measurements were obtained during slightly more active geophysical conditions than in our study (which ranged from ~ 1 to 3). In Table 1, we also include results from Kubota et al. (2011), who observed MSTIDs on 44 nights over central Alaska using OI (630 nm) emission (mean altitude ~ 250 km) during one winter season. They reported strong southward propagation with a significant westward component. The Kp indices for that study were comparable to those by Ishida et al. (2008) (not shown).

Most recently, Frissell et al. (2016) made comprehensive observations of winter/fall daytime MSTIDs using a network of SuperDARN radars located at middle and high latitudes (Table 1). Their measurements, limited to winter/fall, also confirm strong southward propagations for both high- and middle-latitude MSTID events. Figure 11b compares their propagation directions (blue) with our results (gray) over the period from November to April. The southward propagation directions agree exceptionally well; however, our PFISR study indicates more events with an eastward component of propagation. For further comparison, Figure 11c (blue) shows the Kp index for this study in comparison with our study (gray). Although the Ishida et al. (2008) results were obtained under slightly stronger Kp conditions, all three data sets show strong southward wave propagation during the winter months. In addition our PFISR data show strong eastward propagation during the summer months with a clear transition to southeastward during the equinox periods.

6.3. Critical Level Wind and Dissipative Filtering

To investigate the strong seasonal dependence of the observed MSTID propagation directions at PFISR, we considered the effects of critical level wind and dissipative filtering. Winds are expected to be very important in the transmission of the waves on a diurnal, as well as larger scale monthly/seasonal basis. The critical level wind filtering mechanism is well known and affects the spectrum and directionality of the GWs as they propagate upward. In particular, when the observed phase speed of a GW is equal to or less than the wind speed in the direction of the wave, the wave is absorbed into the mean flow (e.g., Booker & Bretherton, 1967; Crowley et al., 1987; Francis, 1973; Fritts, 1978; Hazel, 1967; Hines, 1960; Hines & Reddy, 1967; MacDougall et al., 2009; Vadas, 2007; Waldock & Jones, 1984). Thus, GWs propagating against the wind is favored here, as long as the GW intrinsic period is longer than the buoyancy period. The dissipative filtering mechanism occurs when viscosity is strong, and thus is important in the thermosphere. In this mechanism, those GWs propagating against the wind have larger vertical wavelengths, and therefore are affected much less by molecular viscosity than those GWs propagating with the wind (that have smaller vertical wavelengths). Thus, GW propagation against the wind is also favored in the thermosphere, and these mechanisms work together to eliminate those GWs propagating in the same direction as the wind.

Because there are no direct background wind measurements, we use monthly averaged HWM14 (Drob et al., 2015) meridional and zonal winds. These provide the best available estimate of the dominant recurring background winds and their variability on a monthly basis. This is a large data set and monthly averages can provide an important *first look* at the seasonal variability. We construct blocking diagrams (showing regions where wave propagation is restricted by the winds, e.g., Taylor et al., 1993) as a function of altitude. These diagrams tend to average out diurnal variations. Figure 12 shows the results on a month by month basis. The shaded regions indicate where we would not expect to observe MSTIDs up to an altitude of ~ 300 km, assuming they originated in the lower atmosphere. Also plotted in this figure are the observed phase velocities from each MSTID event (shown as black dots in Figure 12).

During the summer months, the neutral winds are large (~ 200 m/s) and westward, creating a large blocked region in the westward direction. This is consistent with our result that few MSTIDs are seen propagating in this direction. Instead, nearly all the observed MSTID events propagate with a large eastward component. During the winter months, the wind is much smaller (~ 100 m/s) although the blocking direction is west. While some MSTIDs propagate northeastward, no MSTIDs propagate northwestward, and the majority of the waves exhibit strong southward motion. During the equinox months, the neutral winds are ~ 150 m/s and westward. During this time the waves again exhibited eastward propagation, but with an overall southeastward preference; there is little propagation in the northwest quadrant. All of these data are consistent with the effects of critical level and dissipative filtering for the observed GW propagation directions, but this is clearly not the only process controlling the observed distribution (e.g., Crowley & Rodrigues, 2012; Crowley et al., 1987; Del Genio et al., 1979; Francis, 1975; Friedman, 1966; Fritts & Vadas, 2008; Heale et al., 2014; Hines & Hooke, 1970; Klostermeyer, 1972; Pitteway & Hines, 1965; Vadas & Fritts, 2005; Yigit & Medvedev, 2015; Zhang & Yi, 2002). To our best knowledge, this study provides the most conclusive evidence for the effects of the background winds on the MSTIDs.

However, evidence for other systematic effects are also present in Figure 12. Closer examination of the individual MSTID events (black dots) on a month by month basis throughout this 3-year summary suggests a systematic broadening and shrinking in the azimuthal distribution of the wave events during the course of the year. Starting in January the events are nearly all clustered in the SE quadrant, as depicted in Figure 12. By February/March the event cluster has broadened northward and westward in its azimuthal extent, April exhibits further broadening of the azimuthal spread in the events, and by May MSTIDs are seen to propagate

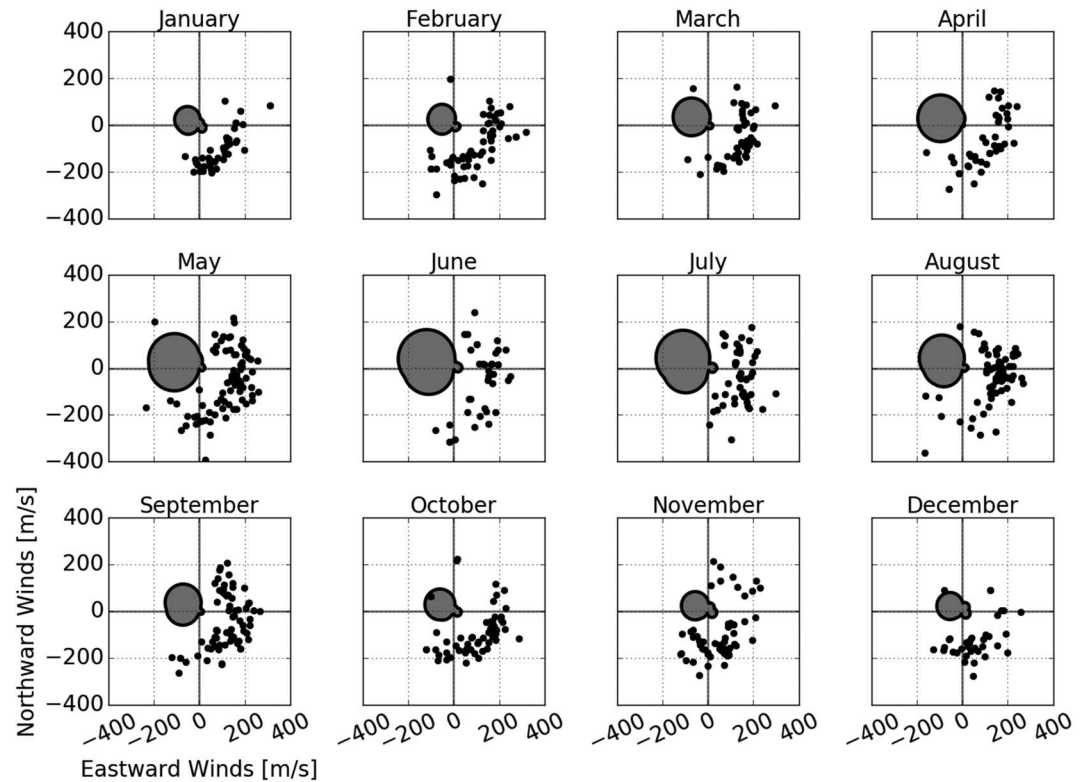


Figure 12. Month by month summary of gravity wave activity and blocking diagrams using HWM14 monthly winds. The 652 medium-scale traveling ionospheric disturbance events are depicted by the black dots.

over all eastward azimuths ranging from 0 to 180°. This general situation prevails throughout the summer months, including September. However, by October/November the azimuthal distribution has reduced significantly with most events propagating in the SE quadrant. By December the distribution resides primarily in the SE quadrant, exhibiting similar characteristics to the January distribution. This additional annual behavior suggesting broadest azimuthal variability during the previously little measured summer period may be associated with seasonal changes in the sources of the MSTIDs and is currently under further investigation.

6.4. Vertical Wavelengths

So far, we have investigated the horizontal parameters of the waves as a function of altitude. As noted in section 4.1, the vertical wave number spectrum has not been determined yet. There are several different methods in the literature previously used to determine the vertical wavelength such as spatial spectral analysis using the vertically pointing beam. However, we have continued with our adapted method of Nicolls and Heinselman (2007) to estimate the vertical wavelength as a function of altitude using the same correlation analysis (as described in section 3.2) but now applied to the vertical pointing beam data. In the Nicolls and Heinselman (2007) study, they compared the measured vertical wavelengths with a (then) recently developed dispersion relation that included the effects of kinematic viscosity and thermal diffusion (e.g., Vadas & Fritts, 2005). The measured vertical wavelengths as a function of altitude for a single MSTID event (average $\lambda_z = 230$ km) were found to be larger than those predicted by the dispersion relation, their Figure 4. For our study, we have continued to use their method to enable a statistical comparison of the vertical wavelengths with those obtained from the dispersion relation using our large data set. We have improved on the Nicolls and Heinselman (2007) method by incorporating daily averaged HWM14 horizontal winds in the dispersion relation. We have also included daily averaged neutral temperatures and densities obtained from the NRLMSISE-00 (e.g., Picone et al., 2002) model which included F10.7 data from NASA's OMNIWeb (Mathews & Towheed, 1995).

Figure 13a shows a histogram of the vertical wavelengths from the PFISR data. The distribution shows a broad peak around 200–300 km, while the majority of the vertical wavelengths are <500 km. In comparison, Figure 13b shows the vertical wavelengths derived from inputting the GW horizontal parameters with winds,

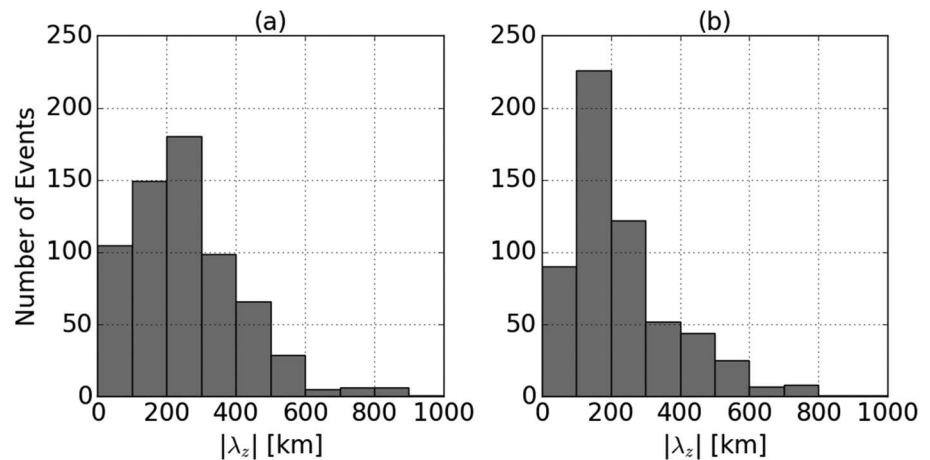


Figure 13. (a) Distribution of measured vertical wavelengths with a mean of 273 km, a median of 216 km, and interquartile range from 124 to 331 km. (b) Vertical wavelengths calculated using a dispersion relation (Vadas & Fritts, 2005) with a mean of 141 km, a median of 133 km, and interquartile range from 93 to 178 km. Neutral temperatures and densities obtained using daily averaged NRLMSISE-00 with F10.7 data from National Aeronautics and Space Administration's OMNIWeb. Neutral winds obtained using daily averaged HWM14 winds.

temperatures, and densities from the HWM14 and NRLMSISE-00 models, respectively, into the GW dissipative dispersion relationship (Vadas & Fritts, 2005). The distributions are clearly very similar, but the dispersion relation peak occurs at somewhat shorter vertical wavelengths ($\sim 150\text{--}200$ km). This difference is likely due to the fact that the neutral winds from HWM14 are climatology winds and have little data in the lower thermosphere (below ~ 220 km) (e.g., Drob et al., 2015; Hedin, 1991) due to lack of measurements; thus, it is not expected that these neutral winds are accurate on an hour-by-hour or day-by-day basis.

Figure 14 builds on this analysis by comparing the distributions of MSTID vertical wavelengths (black line) to those derived from the dispersion relation vertical wavelength (gray line) in 50-km altitude bins. The dispersion vertical wavelengths continue to use HWM14 and NRLMSISE-00 data. The observed and theoretical vertical wavelengths are in reasonable agreement and show a systematic increase in vertical wavelength in altitude. This is consistent with previous observations, which show the vertical wavelength increasing significantly with altitude in the thermosphere (e.g., Djuth et al., 1997; Oliver et al., 1997). It is also consistent with theoretical results (e.g., Vadas, 2007), which show that the increase of the vertical wavelength with altitude occurs because of dissipative filtering of GWs due to kinematic viscosity and thermal diffusivity.

6.5. Kp Versus Propagation Direction

In order to estimate the amount of geomagnetic activity, Figure 15 (gray dots) shows a 30-day running mean of daily averaged AE indices over the time periods from December 2010 to December 2011 (Figure 15a) and from February 2012 to December 2012 (Figure 15c), obtained from NASA's OMNIWeb (Mathews & Towheed, 1995). A visual comparison with the 30-day running mean of the AE indices and wave azimuth suggests a correlation between the magnitude of the AE and the dominant wave propagation direction during this 32-month study, which was composed of nine seasonal changes. To better quantify this possible relationship, Figures 15a and 15c show the results of a correlation analysis between these two data sets. The daily averaged propagation directions were calculated with a 30-day running average. The propagation directions (black dots) along with AE indices (gray dots) show remarkable agreement in both the broad (several month) and finer scale (month to month) structure and relative changes. A Pearson correlation analysis results in a coefficient of 0.64 during the year 2011 and 0.5 during the year 2012. This is an intriguing result, because there have been many studies investigating the relationship between the occurrence of MSTIDs with geophysical activity (e.g., Chimonas & Hines, 1970; Crowley et al., 1987; Francis, 1974, 1975; Frissell et al., 2014, 2016; Grocott et al., 2013; He et al., 2004). For example, Frissell et al. (2016) investigated whether or not space weather had an effect on MSTID occurrence. They concluded that the AE and SYM-H indices did not correlate with MSTID occurrence. The new availability of year-round MSTID measurements as presented herein has opened the door to new correlative investigations. This is further illustrated in Figures 15b and 15c, which show a histogram of the number of hours of observations of MSTIDs to the number of hours of PFISR observations.

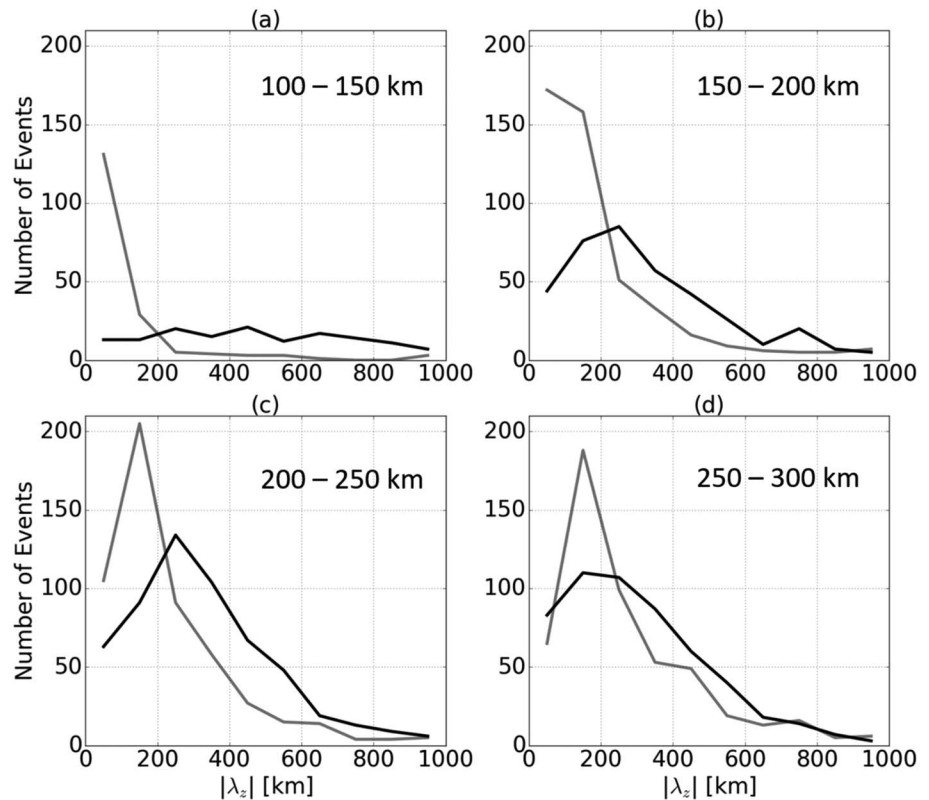


Figure 14. Distributions of the measured vertical wavelenghts (black) versus dispersion vertical wavelenghts (gray), calculated using HWM14 background winds and NRLMSISE-00 neutral temperatures and densities, in 50-km-altitude bins.

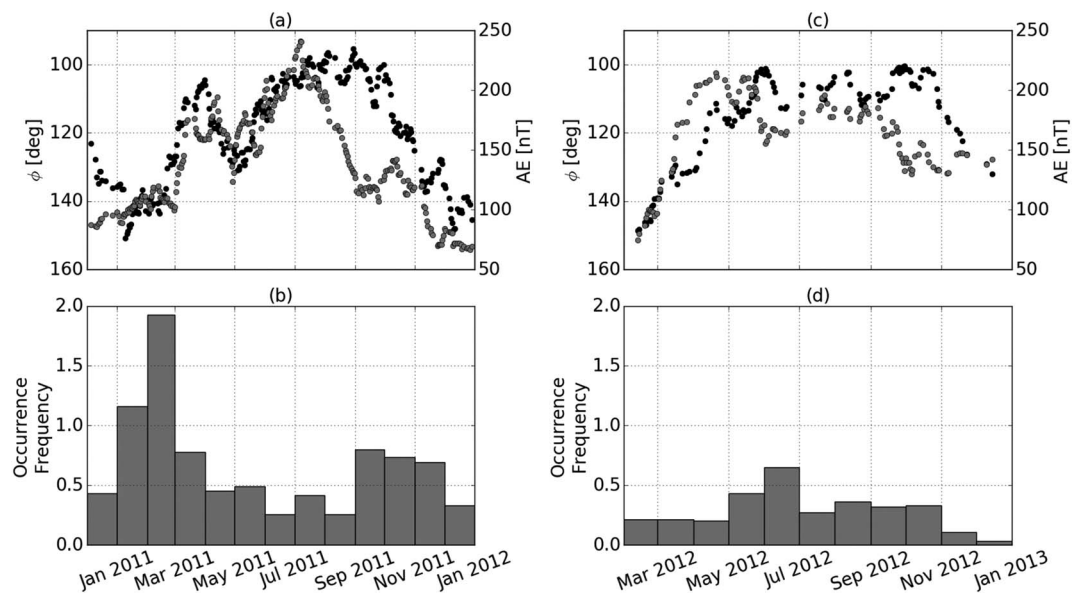


Figure 15. Daily averaged propagation directions with 30-day running average (black dots) and daily averaged AE indices from NASA's OMNIWeb with 30-day running average (gray dots) for the periods from (a) December 2010–2011 and (c) February 2012 to December 2012. Plots (b) and (d) show the ratio of the number of hours of MSTID observations to the total number of PFISR observations during these time periods. MSTID = medium-scale traveling ionospheric disturbance; PFISR = Poker Flat Incoherent Scatter Radar.

7. Summary

Over 650 MSTID events were observed by PFISR over a ~3-year period enabling a comprehensive study of their characteristics and seasonal variabilities. We have determined the observed period, horizontal wavelength, phase speed, and propagation directions as a function of altitude (ranging from 100 to 300 km) for all these events. The altitude-averaged periods exhibited a mean of 41 min with interquartile ranges from ~37 to 44 min, horizontal wavelengths with a mean of 446 km ranging from ~369 to 514 km, and phase speeds with a mean of 187 m/s ranging from 155 to 212 m/s. The wave periods and azimuths were found to be nearly constant with altitude, while both the horizontal wavelengths and the phase speeds exhibited ~20% increase with altitude.

The distribution of vertical wavelengths exhibits a broad peak around 200–300 km, with the majority of the vertical wavelengths <500 km. These measured vertical wavelengths are compared with calculated vertical wavelengths using a thermospheric GW dissipative dispersion relation (e.g., Vadas & Fritts, 2005). The distributions are very similar, but the dispersion relation peak occurs at somewhat shorter vertical wavelengths (~150–200 km). We also investigated the vertical wavelengths as a function of altitude for all MSTID events. The observed and theoretical vertical wavelengths are in reasonable agreement and show a systematic increase with altitude.

The altitude-averaged observed wave periods, horizontal wavelengths, and phase speeds are consistent over the course of this 32-month study, while the propagation directions reveals striking seasonal changes in the dominant wave propagation directions. During the summer months the waves exhibit a strong preference for eastward propagation. In contrast, the MSTIDs observed during the winter months propagate southward. The equinox periods show a preference for wave propagation toward the southeast, in between the primary directions of winter and summer seasons. Together, these data suggest a consistent cyclic picture with eastward propagation during the summer months, transitioning to southeastward during the equinox periods and then to predominantly southward during the winter seasons. Thereafter, the cycle reversed back to eastward during the summer. Our novel seasonal findings build and extend on the results of Ishida et al. (2008) and Frissell et al. (2016) who used SuperDARN daytime HF radar data to determine strong southward MSTID propagation during the winter/fall periods only.

The effects of critical level wind and dissipative filtering of the MSTID propagation directions were investigated using the HWM14 winds. Blocking diagrams show the blocked region toward the west during all seasons and agrees with our results of eastward wave propagation. To our best knowledge, this study provides the most conclusive evidence for the effects of seasonal background winds on the MSTIDs. In future, the local time variations of the individual TIDs and the local time effects of the varying wind field will be investigated.

In conjunction with the strong summertime eastward propagation peak, there is also a large broadening in the azimuthal spread of the observed MSTIDs. This spread systematically reduces during the equinox periods to a minimum in the winter season where the MSTIDs are most highly focused on southward propagation. This additional finding together with the observed near total lack of waves propagating westward points toward (even under reduced wind blocking conditions) strongly suggests additional causes of the observed propagation anisotropy, most likely associated with the wave sources, which are currently under investigation.

Finally, there have been many studies investigating the relationship between the occurrence of MSTIDs with geophysical activity. In this study we have identified an unexpected strong correlation between the MSTID propagation directions and the AE index, which is also under further investigation.

References

- Afraimovich, E. L., Boitman, O. N., Zhovty, E. I., Kalikhman, A. D., & Pirog, T. G. (1999). Dynamics and anisotropy of traveling ionospheric disturbances as deduced from transionospheric sounding data. *Radio Science*, *34*(2), 477–487. <https://doi.org/10.1029/1998RS900004>
- Afraimovich, E., Voeykov, S., Perevalova, N., & Ratovsky, K. (2008). Large-scale traveling ionospheric disturbances of auroral origin according to the data of the GPS network and ionosondes. *Advances in Space Research*, *42*(7), 1213–1217. <https://doi.org/10.1016/j.asr.2007.11.023>
- Bauer, S. J. (1958). An apparent ionospheric response to the passage of hurricanes. *Journal of Geophysical Research*, *63*(1), 265–269. <https://doi.org/10.1029/JZ063i001p00265>
- Bishop, R. L., Aponte, N., Earle, G. D., Sulzer, M., Larsen, M. F., & Peng, G. S. (2006). Arecibo observations of ionospheric perturbations associated with the passage of tropical storm Odette. *Journal of Geophysical Research*, *111*, A11320. <https://doi.org/10.1029/2006JA011668>
- Booker, J. R., & Bretherton, F. P. (1967). The critical layer for internal gravity waves in a shear flow. *Journal of Fluid Mechanics*, *27*(3), 513–539. <https://doi.org/10.1017/S0022112067000515>
- Bristow, W. A., & Greenwald, R. A. (1996). Multiradar observations of medium-scale acoustic gravity waves using the Super Dual Auroral Radar Network. *Journal of Geophysical Research*, *101*(A11), 24,499–24,511. <https://doi.org/10.1029/96JA01494>

Acknowledgments

The Utah State University Center for Atmospheric and Space Sciences (CASS) acknowledges the support of the NSF Graduate Research Fellowship under grant 1147384 supporting M. R. Negale's graduate research program. The PFISR IPY data used in this extensive analysis are available online through Open Madrigal (<http://www.openmadrigal.org>). OMNIWeb was accessed through the NASA Space Physics Data Facility (<https://omniweb.gsfc.nasa.gov>). We acknowledge the use of Free Open Source Software projects used in this analysis: primarily Python, Matplotlib, NumPy, SciPy, and Pandas. S. L. V. was supported by NSF grants AGS-1552315, AGS-1452329, and AGS-1242897. We thank the ALOMAR Observatory facilities and staff for supporting our AMTM measurements obtained as part of NSF grant AGS 1042227. M.J.T was supported (in part) under NSF OPP grant 1443730. We gratefully acknowledge the considerable help of Y. Zhao and P.-D. Pautet, CASS, during the course of this investigation.

- Bristow, W. A., Greenwald, R. A., & Samson, J. C. (1994). Identification of high-latitude acoustic gravity wave sources using the Goose Bay HF radar. *Journal of Geophysical Research*, *99*(A1), 319–331. <https://doi.org/10.1029/93JA01470>
- Chimonas, G., & Hines, C. (1970). Atmospheric gravity waves launched by auroral currents. *Planetary and Space Science*, *18*(4), 565–582. [https://doi.org/10.1016/0032-0633\(70\)90132-7](https://doi.org/10.1016/0032-0633(70)90132-7)
- Chisham, G., Lester, M., Milan, S. E., Freeman, M. P., Bristow, W. A., Grocott, A., et al. (2007). A decade of the Super Dual Auroral Radar Network (SuperDARN): Scientific achievements, new techniques and future directions. *Surveys in Geophysics*, *28*(1), 33–109. <https://doi.org/10.1007/s10712-007-9017-8>
- Crowley, G., Jones, T., & Dudeney, J. (1987). Comparison of short period TID morphologies in Antarctica during geomagnetically quiet and active intervals. *Journal of Atmospheric and Terrestrial Physics*, *49*(11), 1155–1162. [https://doi.org/10.1016/0021-9169\(87\)90098-5](https://doi.org/10.1016/0021-9169(87)90098-5)
- Crowley, G., & Rodrigues, F. S. (2012). Characteristics of traveling ionospheric disturbances observed by the TIDDBIT sounder. *Radio Science*, *47*, RS0L22. <https://doi.org/10.1029/2011RS004959>
- Davies, K., & Baker, D. M. (1965). Ionospheric effects observed around the time of the Alaskan earthquake of March 28, 1964. *Journal of Geophysical Research*, *70*(9), 2251–2253. <https://doi.org/10.1029/JZ070i009p02251>
- Davies, K., & Jones, J. (1973). Acoustic waves in the ionospheric F2-region produced by severe thunderstorms. *Journal of Atmospheric and Terrestrial Physics*, *35*(10), 1737–1744. [https://doi.org/10.1016/0021-9169\(73\)90052-4](https://doi.org/10.1016/0021-9169(73)90052-4)
- Del Genio, A. D., Schubert, G., & Straus, J. M. (1979). Gravity wave propagation in a diffusively separated atmosphere with height-dependent collision frequencies. *Journal of Geophysical Research*, *84*(A8), 4371–4378. <https://doi.org/10.1029/JA084iA08p04371>
- Ding, F., Wan, W., Xu, G., Yu, T., Yang, G., & Wang, J.-s. (2011). Climatology of medium-scale traveling ionospheric disturbances observed by a GPS network in central China. *Journal of Geophysical Research*, *116*, A09327. <https://doi.org/10.1029/2011JA016545>
- Djuth, F. T., Sulzer, M. P., & Elder, J. H. (1994). Application of the coded long-pulse technique to plasma line studies of the ionosphere. *Geophysical Research Letters*, *21*(24), 2725–2728. <https://doi.org/10.1029/94GL01699>
- Djuth, F. T., Sulzer, M. P., Elder, J. H., & Wickwar, V. B. (1997). High-resolution studies of atmosphere-ionosphere coupling at Arecibo Observatory, Puerto Rico. *Radio Science*, *32*(6), 2321–2344. <https://doi.org/10.1029/97RS02797>
- Drob, D. P., Emmert, J. T., Meriwether, J. W., Makela, J. J., Doornbos, E., Conde, M., et al. (2015). An update to the Horizontal Wind Model (HWM): The quiet time thermosphere. *Earth and Space Science*, *2*, 301–319. <https://doi.org/10.1002/2014EA000089>
- Evans, J., Holt, J., & Wand, R. (1983). A differential-Doppler study of traveling ionospheric disturbances from Millstone Hill. *Radio Science*, *18*(3), 435–451.
- Fedorenko, A. K., & Kryuchkov, E. I. (2013). Wind control of the propagation of acoustic gravity waves in the polar atmosphere. *Geomagnetism and Aeronomy*, *53*(3), 377–388. <https://doi.org/10.1134/S0016793213030055>
- Francis, S. H. (1973). Lower-atmospheric gravity modes and their relation to medium-scale traveling ionospheric disturbances. *Journal of Geophysical Research*, *78*(34), 8289–8295. <https://doi.org/10.1029/JA078i034p08289>
- Francis, S. H. (1974). A theory of medium-scale traveling ionospheric disturbances. *Journal of Geophysical Research*, *79*(34), 5245–5260. <https://doi.org/10.1029/JA079i034p05245>
- Francis, S. H. (1975). Global propagation of atmospheric gravity waves: A review. *Journal of Atmospheric and Terrestrial Physics*, *37*(6), 1011–1054. [https://doi.org/10.1016/0021-9169\(75\)90012-4](https://doi.org/10.1016/0021-9169(75)90012-4)
- Friedman, J. P. (1966). Propagation of internal gravity waves in a thermally stratified atmosphere. *Journal of Geophysical Research*, *71*(4), 1033–1054. <https://doi.org/10.1029/JZ071i004p01033>
- Frissell, N. A., Baker, J., Ruohoniemi, J. M., Gerrard, A. J., Miller, E. S., Marini, J. P., et al. (2014). Climatology of medium-scale traveling ionospheric disturbances observed by the midlatitude Blackstone SuperDARN radar. *Journal of Geophysical Research: Space Physics*, *119*, 7679–7697. <https://doi.org/10.1002/2014JA019870>
- Frissell, N. A., Baker, J. B. H., Ruohoniemi, J. M., Greenwald, R. A., Gerrard, A. J., Miller, E. S., & West, M. L. (2016). Sources and characteristics of medium-scale traveling ionospheric disturbances observed by high-frequency radars in the North American sector. *Journal of Geophysical Research: Space Physics*, *121*, 3722–3739. <https://doi.org/10.1002/2015JA022168>
- Fritts, D. C. (1978). The nonlinear gravity wave-critical level interaction. *Journal of the Atmospheric Sciences*, *35*(3), 397–413. [https://doi.org/10.1175/1520-0469\(1978\)035<0397:TNGWCL>2.0.CO;2](https://doi.org/10.1175/1520-0469(1978)035<0397:TNGWCL>2.0.CO;2)
- Fritts, D. C., & Alexander, M. J. (2003). Gravity wave dynamics and effects in the middle atmosphere. *Reviews of Geophysics*, *41*(1), 1003. <https://doi.org/10.1029/2001RG000106>
- Fritts, D. C., & Vadas, S. L. (2008). Gravity wave penetration into the thermosphere: Sensitivity to solar cycle variations and mean winds. *Annales de Geophysique*, *26*(12), 3841–3861. <https://doi.org/10.5194/angeo-26-3841-2008>
- Fukao, S., Yamamoto, Y., Oliver, W. L., Takami, T., Yamanaka, M. D., Yamamoto, M., et al. (1993). Middle and upper atmosphere radar observations of ionospheric horizontal gradients produced by gravity waves. *Journal of Geophysical Research*, *98*(A6), 9443–9451. <https://doi.org/10.1029/92JA02846>
- Galushko, V. G., Paznukhov, V. V., Sopin, A. A., & Yampolski, Y. M. (2016). Statistics of ionospheric disturbances over the Antarctic Peninsula as derived from TEC measurements. *Journal of Geophysical Research: Space Physics*, *121*, 3395–3409. <https://doi.org/10.1002/2015JA022302>
- Garcia, R. R., & Solomon, S. (1985). The effect of breaking gravity waves on the dynamics and chemical composition of the mesosphere and lower thermosphere. *Journal of Geophysical Research*, *90*(D2), 3850–3868. <https://doi.org/10.1029/JD090iD02p03850>
- Georges, T. M. (1967). Evidence for the influence of atmospheric waves on ionospheric motions. *Journal of Geophysical Research*, *72*(1), 422–425. <https://doi.org/10.1029/JZ072i001p00422>
- Georges, T. M. (1968). HF doppler studies of traveling ionospheric disturbances. *Journal of Atmospheric and Terrestrial Physics*, *30*(5), 735–746. [https://doi.org/10.1016/S0021-9169\(68\)80029-7](https://doi.org/10.1016/S0021-9169(68)80029-7)
- Gossard, E. E. (1962). Vertical flux of energy into the lower ionosphere from internal gravity waves generated in the troposphere. *Journal of Geophysical Research*, *67*(2), 745–757. <https://doi.org/10.1029/JZ067i002p00745>
- Greenwald, R. A., Baker, K. B., Dudeney, J. R., Pinnock, M., Jones, T. B., Thomas, E. C., et al. (1995). DARN/SuperDARN. *Space Science Reviews*, *71*(1), 761–796. <https://doi.org/10.1007/BF00751350>
- Grocott, A., Hosokawa, K., Ishida, T., Lester, M., Milan, S. E., Freeman, M. P., et al. (2013). Characteristics of medium-scale traveling ionospheric disturbances observed near the Antarctic Peninsula by HF radar. *Journal of Geophysical Research: Space Physics*, *118*, 5830–5841. <https://doi.org/10.1002/jgra.50515>
- Hazel, P. (1967). The effect of viscosity and heat conduction on internal gravity waves at a critical level. *Journal of Fluid Mechanics*, *30*(4), 775–783. <https://doi.org/10.1017/S0022112067001752>
- He, L.-S., Dyson, P., Parkinson, M., & Wan, W. (2004). Studies of medium scale travelling ionospheric disturbances using TIGER SuperDARN radar sea echo observations. *Annales Geophysicae*, *22*, 4077–4088.
- Heale, C. J., Snively, J. B., Hickey, M. P., & Ali, C. J. (2014). Thermospheric dissipation of upward propagating gravity wave packets. *Journal of Geophysical Research: Space Physics*, *119*, 3857–3872. <https://doi.org/10.1002/2013JA019387>

- Hedin, A. E. (1991). Extension of the MSIS thermosphere model into the middle and lower atmosphere. *Journal of Geophysical Research*, 96(A2), 1159–1172. <https://doi.org/10.1029/90JA02125>
- Heinselman, C. J., & Nicolls, M. J. (2008). A Bayesian approach to electric field and E-region neutral wind estimation with the Poker Flat Advanced Modular Incoherent Scatter Radar. *Radio Science*, 43, RS5013. <https://doi.org/10.1029/2007RS003805>
- Hernández-Pajares, M., Juan, J. M., Sanz, J., & Aragón-Ángel, A. (2012). Propagation of medium scale traveling ionospheric disturbances at different latitudes and solar cycle conditions. *Radio Science*, 47, RS0K05. <https://doi.org/10.1029/2011RS004951>
- Hines, C. O. (1960). Internal atmospheric gravity waves at ionospheric heights. *Canadian Journal of Physics*, 38(11), 1441–1481. <https://doi.org/10.1139/p60-150>
- Hines, C. O., & Hooke, W. H. (1970). Discussion of ionization effects on the propagation of acoustic-gravity waves in the ionosphere. *Journal of Geophysical Research*, 75(13), 2563–2568. <https://doi.org/10.1029/JA075i013p02563>
- Hines, C. O., & Reddy, C. A. (1967). On the propagation of atmospheric gravity waves through regions of wind shear. *Journal of Geophysical Research*, 72(3), 1015–1034. <https://doi.org/10.1029/JZ072i003p01015>
- Hocke, K., & Schlegel, K. (1996). A review of atmospheric gravity waves and travelling ionospheric disturbances: 1982–1995. *Annales Geophysicae*, 14, 917–940.
- Hocke, K., & Tsuda, T. (2001). Gravity waves and ionospheric irregularities over tropical convection zones observed by GPS/MET radio occultation. *Geophysical Research Letters*, 28(14), 2815–2818. <https://doi.org/10.1029/2001GL013076>
- Holton, J. R. (1982). The role of gravity wave induced drag and diffusion in the momentum budget of the mesosphere. *Journal of the Atmospheric Sciences*, 39(4), 791–799. [https://doi.org/10.1175/1520-0469\(1982\)039<0791:TROGWI>2.0.CO;2](https://doi.org/10.1175/1520-0469(1982)039<0791:TROGWI>2.0.CO;2)
- Holton, J. R. (1983). The influence of gravity wave breaking on the general circulation of the middle atmosphere. *Journal of the Atmospheric Sciences*, 40(10), 2497–2507. [https://doi.org/10.1175/1520-0469\(1983\)040<2497:TIOGWB>2.0.CO;2](https://doi.org/10.1175/1520-0469(1983)040<2497:TIOGWB>2.0.CO;2)
- Hooke, W. (1968). Ionospheric irregularities produced by internal atmospheric gravity waves. *Journal of Atmospheric and Terrestrial Physics*, 30(5), 795–823. [https://doi.org/10.1016/S0021-9169\(68\)80033-9](https://doi.org/10.1016/S0021-9169(68)80033-9)
- Huang, C.-S., & Kelley, M. C. (1996). Nonlinear evolution of equatorial spread F: 4. Gravity waves, velocity shear, and day-to-day variability. *Journal of Geophysical Research*, 101(A11), 24,521–24,532. <https://doi.org/10.1029/96JA02332>
- Huang, C.-S., Kelley, M. C., & Hysell, D. L. (1993). Nonlinear Rayleigh-Taylor instabilities, atmospheric gravity waves and equatorial spread F. *Journal of Geophysical Research*, 98(A9), 15,631–15,642. <https://doi.org/10.1029/93JA00762>
- Hung, R., & Kuo, J. (1978). Ionospheric observation of gravity-waves associated with hurricane Eloise. *Journal of Geophysics Zeitschrift für Geophysik*, 45(1), 67–80.
- Hung, R. J., Phan, T., & Smith, R. E. (1979). Coupling of ionosphere and troposphere during the occurrence of isolated tornadoes on November 20, 1973. *Journal of Geophysical Research*, 84(A4), 1261–1268. <https://doi.org/10.1029/JA084iA04p01261>
- Hung, R. J., & Smith, R. E. (1978). Ray tracing of gravity waves as a possible warning system for tornadic storms and hurricanes. *Journal of Applied Meteorology*, 17(1), 3–11. [https://doi.org/10.1175/1520-0450\(1978\)017<0003:RTOGWA>2.0.CO;2](https://doi.org/10.1175/1520-0450(1978)017<0003:RTOGWA>2.0.CO;2)
- Hunsucker, R. D. (1982). Atmospheric gravity waves generated in the high-latitude ionosphere: A review. *Reviews of Geophysics*, 20(2), 293–315. <https://doi.org/10.1029/RG020i002p00293>
- Hysell, D. L., Kelley, M. C., Swartz, W. E., & Woodman, R. F. (1990). Seeding and layering of equatorial spread F by gravity waves. *Journal of Geophysical Research*, 95(A10), 17,253–17,260. <https://doi.org/10.1029/JA095iA10p17253>
- Ishida, T., Hosokawa, K., Shibata, T., Suzuki, S., Nishitani, N., & Ogawa, T. (2008). SuperDARN observations of daytime MSTIDs in the auroral and mid-latitudes: Possibility of long-distance propagation. *Geophysical Research Letters*, 35, L13102. <https://doi.org/10.1029/2008GL034623>
- Kelley, M. C. (1997). In situ ionospheric observations of severe weather-related gravity waves and associated small-scale plasma structure. *Journal of Geophysical Research*, 102(A1), 329–335. <https://doi.org/10.1029/96JA03033>
- Klostermeyer, J. (1972). Numerical calculation of gravity wave propagation in a realistic thermosphere. *Journal of Atmospheric and Terrestrial Physics*, 34(5), 765–774. [https://doi.org/10.1016/0021-9169\(72\)90109-2](https://doi.org/10.1016/0021-9169(72)90109-2)
- Kotake, N., Otsuka, Y., Ogawa, T., Tsugawa, T., & Saito, A. (2007). Statistical study of medium-scale traveling ionospheric disturbances observed with the GPS networks in Southern California. *Earth Planet Space*, 59(2), 95–102. <https://doi.org/10.1186/BF03352681>
- Kubota, M., Conde, M., Ishii, M., Murayama, Y., & Jin, H. (2011). Characteristics of nighttime medium-scale traveling ionospheric disturbances observed over Alaska. *Journal of Geophysical Research*, 116, A05307. <https://doi.org/10.1029/2010JA016212>
- Lindzen, R. S. (1981). Turbulence and stress owing to gravity wave and tidal breakdown. *Journal of Geophysical Research*, 86(C10), 9707–9714. <https://doi.org/10.1029/JC086iC10p09707>
- Ma, S. Y., Schlegel, K., & Xu, J. S. (1998). Case studies of the propagation characteristics of auroral TIDs with EISCAT CP2 data using maximum entropy cross-spectral analysis. *Annales de Geophysique*, 16(2), 161–167. <https://doi.org/10.1007/s00585-998-0161-3>
- MacDougall, J., Li, G., & Jayachandran, P. (2009). Traveling ionospheric disturbances near London, Canada. *Journal of Atmospheric and Solar-Terrestrial Physics*, 71(17), 2077–2084. <https://doi.org/10.1016/j.jastp.2009.09.016>
- Mathews, G., & Towheed, S. S. (1995). NSSDC OMNIWeb: The first space physics WWW-based data browsing and retrieval system. *Computer Networks and ISDN Systems*, 27(6), 801–808. [https://doi.org/10.1016/0169-7552\(95\)00033-4](https://doi.org/10.1016/0169-7552(95)00033-4)
- Morgan, M. G., Calderón, C. H. J., & Ballard, K. A. (1978). Techniques for the study of TID's with multi-station rapid-run ionosondes. *Radio Science*, 13(4), 729–741. <https://doi.org/10.1029/RS013i004p00729>
- Munro, G. (1948). Short-period changes in the F region of the ionosphere. *Nature*, 162(4127), 886–887.
- Nicolls, M. J., & Heinselman, C. J. (2007). Three-dimensional measurements of traveling ionospheric disturbances with the Poker Flat Incoherent Scatter Radar. *Geophysical Research Letters*, 34, L21104. <https://doi.org/10.1029/2007GL031506>
- Nicolls, M. J., Kelley, M. C., Coster, A. J., González, S. A., & Makela, J. J. (2004). Imaging the structure of a large-scale TID using ISR and TEC data. *Geophysical Research Letters*, 31, L09812. <https://doi.org/10.1029/2004GL019797>
- Nicolls, M. J., Vadas, S. L., Aponte, N., & Sulzer, M. P. (2014). Horizontal parameters of daytime thermospheric gravity waves and E region neutral winds over Puerto Rico. *Journal of Geophysical Research: Space Physics*, 119, 575–600. <https://doi.org/10.1002/2013JA018988>
- Ogawa, T., Igarashi, K., Aikyo, K., & Maeno, H. (1987). NNSS satellite observations of medium-scale traveling ionospheric disturbances at southern high-latitudes. *Journal of Geomagnetism and Geoelectricity*, 39(12), 709–721. <https://doi.org/10.5636/jgg.39.709>
- Ogawa, T., Nishitani, N., Otsuka, Y., Shiokawa, K., Tsugawa, T., & Hosokawa, K. (2009). Medium-scale traveling ionospheric disturbances observed with the SuperDARN Hokkaido radar, all-sky imager, and GPS network and their relation to concurrent sporadic E irregularities. *Journal of Geophysical Research*, 114, A03316. <https://doi.org/10.1029/2008JA013893>
- Oliver, W. L., Otsuka, Y., Sato, M., Takami, T., & Fukao, S. (1997). A climatology of F region gravity wave propagation over the middle and upper atmosphere radar. *Journal of Geophysical Research*, 102(A7), 14,499–14,512. <https://doi.org/10.1029/97JA00491>
- Onishi, T., Tsugawa, T., Otsuka, Y., Berthelier, J.-J., & Lebreton, J.-P. (2009). First simultaneous observations of daytime MSTIDs over North America using GPS-TEC and DEMETER satellite data. *Geophysical Research Letters*, 36, L11808. <https://doi.org/10.1029/2009GL038156>

- Paulino, I., Medeiros, A., Vadas, S., Wrasse, C., Takahashi, H., Buriti, R., et al. (2016). Periodic waves in the lower thermosphere observed by OI630 nm airglow images. *Annales de Geophysique*, 34(2), 293–301.
- Picone, J. M., Hedin, A. E., Drob, D. P., & Aikin, A. C. (2002). NRLMSISE-00 empirical model of the atmosphere: Statistical comparisons and scientific issues. *Journal of Geophysical Research*, 107(A12), 1468. <https://doi.org/10.1029/2002JA009430>
- Pinger, W. H. (1979). Detection of traveling ionospheric disturbances with auroral zone incoherent scatter radar. *Radio Science*, 14(1), 75–84. <https://doi.org/10.1029/RS014i001p00075>
- Pitteway, M. L. V., & Hines, C. O. (1965). The reflection and ducting of atmospheric acoustic-gravity waves. *Canadian Journal of Physics*, 43(12), 2222–2243. <https://doi.org/10.1139/p65-217>
- Prasad, S. S., Schneck, L. J., & Davies, K. (1975). Ionospheric disturbances by severe tropospheric weather storms. *Journal of Atmospheric and Terrestrial Physics*, 37(10), 1357–1363. [https://doi.org/10.1016/0021-9169\(75\)90128-2](https://doi.org/10.1016/0021-9169(75)90128-2)
- Ratovsky, K., Medvedev, A., Tolstikov, M., & Kushnarev, D. (2008). Case studies of height structure of TID propagation characteristics using cross-correlation analysis of incoherent scatter radar and DPS-4 ionosonde data. *Advances in Space Research*, 41(9), 1454–1458. <https://doi.org/10.1016/j.asr.2007.03.008>
- Reid, I. (1986). Gravity wave motions in the upper middle atmosphere (60–110 km). *Journal of Atmospheric and Terrestrial Physics*, 48(11), 1057–1072. [https://doi.org/10.1016/0021-9169\(86\)90026-7](https://doi.org/10.1016/0021-9169(86)90026-7)
- Richmond, A. D. (1978). Gravity wave generation, propagation, and dissipation in the thermosphere. *Journal of Geophysical Research*, 83(A9), 4131–4145. <https://doi.org/10.1029/JA083iA09p04131>
- Röttger, J. (1977). Travelling disturbances in the equatorial ionosphere and their association with penetrative cumulus convection. *Journal of Atmospheric and Terrestrial Physics*, 39(9), 987–998. [https://doi.org/10.1016/0021-9169\(77\)90007-1](https://doi.org/10.1016/0021-9169(77)90007-1)
- Samson, J. C., Greenwald, R. A., Ruohoniemi, J. M., & Baker, K. B. (1989). High-frequency radar observations of atmospheric gravity waves in the high-latitude ionosphere. *Geophysical Research Letters*, 16(8), 875–878. <https://doi.org/10.1029/GL016i008p00875>
- Samson, J. C., Greenwald, R. A., Ruohoniemi, J. M., Frey, A., & Baker, K. B. (1990). Goose Bay radar observations of Earth-reflected, atmospheric gravity waves in the high-latitude ionosphere. *Journal of Geophysical Research*, 95(A6), 7693–7709. <https://doi.org/10.1029/JA095iA06p07693>
- Sekar, R., & Kelley, M. C. (1998). On the combined effects of vertical shear and zonal electric field patterns on nonlinear equatorial spread F evolution. *Journal of Geophysical Research*, 103(A9), 20,735–20,747. <https://doi.org/10.1029/98JA01561>
- Sekar, R., Suhasini, R., & Raghavarao, R. (1995). Evolution of plasma bubbles in the equatorial F region with different seeding conditions. *Geophysical Research Letters*, 22(8), 885–888. <https://doi.org/10.1029/95GL00813>
- Shiokawa, K., Ihara, C., Otsuka, Y., & Ogawa, T. (2003). Statistical study of nighttime medium-scale traveling ionospheric disturbances using midlatitude airglow images. *Journal of Geophysical Research*, 108(A1), 1052. <https://doi.org/10.1029/2002JA009491>
- Shiokawa, K., Otsuka, Y., & Ogawa, T. (2009). Propagation characteristics of nighttime mesospheric and thermospheric waves observed by optical mesosphere thermosphere imagers at middle and low latitudes. *Earth Planet Space*, 61(4), 479–491. <https://doi.org/10.1186/BF03353165>
- Sojka, J., Nicolls, M., Heinselman, C., & Kelly, J. (2009). The PFISR IPY observations of ionospheric climate and weather. *Journal of Atmospheric and Solar-Terrestrial Physics*, 71(6), 771–785. <https://doi.org/10.1016/j.jastp.2009.01.001>
- Taylor, M. J., Jahn, J.-M., Fukao, S., & Saito, A. (1998). Possible evidence of gravity wave coupling into the mid-latitude F region ionosphere during the SEEK campaign. *Geophysical Research Letters*, 25(11), 1801–1804. <https://doi.org/10.1029/97GL03448>
- Taylor, M. J., Ryan, E. H., Tuan, T. F., & Edwards, R. (1993). Evidence of preferential directions for gravity wave propagation due to wind filtering in the middle atmosphere. *Journal of Geophysical Research*, 98(A4), 6047–6057. <https://doi.org/10.1029/92JA02604>
- Tedd, B. L., Morgan, M. G., & Ballard, K. A. (1984). The height dependence of TID and gravity wave parameters. *Journal of Geophysical Research*, 89(A10), 9023–9033. <https://doi.org/10.1029/JA089iA10p09023>
- Testud, J. (1970). Gravity waves generated during magnetic substorms. *Journal of Atmospheric and Terrestrial Physics*, 32(11), 1793–1805. [https://doi.org/10.1016/0021-9169\(70\)90137-6](https://doi.org/10.1016/0021-9169(70)90137-6)
- Vadas, S. L. (2007). Horizontal and vertical propagation and dissipation of gravity waves in the thermosphere from lower atmospheric and thermospheric sources. *Journal of Geophysical Research*, 112, A06305. <https://doi.org/10.1029/2006JA011845>
- Vadas, S. L., & Crowley, G. (2010). Sources of the traveling ionospheric disturbances observed by the ionospheric TIDBIT sounder near Wallops Island on 30 October 2007. *Journal of Geophysical Research*, 115, A07324. <https://doi.org/10.1029/2009JA015053>
- Vadas, S. L., & Fritts, D. C. (2005). Thermospheric responses to gravity waves: Influences of increasing viscosity and thermal diffusivity. *Journal of Geophysical Research*, 110, D15103. <https://doi.org/10.1029/2004JD005574>
- Vadas, S. L., & Liu, H.-I. (2009). Generation of large-scale gravity waves and neutral winds in the thermosphere from the dissipation of convectively generated gravity waves. *Journal of Geophysical Research*, 114, A10310. <https://doi.org/10.1029/2009JA014108>
- Vadas, S. L., & Liu, H.-I. (2013). Numerical modeling of the large-scale neutral and plasma responses to the body forces created by the dissipation of gravity waves from 6 h of deep convection in Brazil. *Journal of Geophysical Research: Space Physics*, 118, 2593–2617. <https://doi.org/10.1002/jgra.50249>
- Vadas, S. L., Liu, H.-I., & Lieberman, R. S. (2014). Numerical modeling of the global changes to the thermosphere and ionosphere from the dissipation of gravity waves from deep convection. *Journal of Geophysical Research: Space Physics*, 119, 7762–7793. <https://doi.org/10.1002/2014JA020280>
- Vadas, S. L., & Nicolls, M. J. (2008). Using PFISR measurements and gravity wave dissipative theory to determine the neutral, background thermospheric winds. *Geophysical Research Letters*, 35, L02105. <https://doi.org/10.1029/2007GL031522>
- Vadas, S. L., & Nicolls, M. J. (2009). Temporal evolution of neutral, thermospheric winds and plasma response using PFISR measurements of gravity waves. *Journal of Atmospheric and Solar-Terrestrial Physics*, 71(6), 744–770. <https://doi.org/10.1016/j.jastp.2009.01.011>
- Vlasov, A., Kauristie, K., van de Kamp, M., Luntama, J.-P., & Pogoreltsev, A. (2011). A study of traveling ionospheric disturbances and atmospheric gravity waves using EISCAT Svalbard radar IPY-data. *Annales Geophysicae*, 29, 2101.
- Waldock, J., & Jones, T. (1984). The effects of neutral winds on the propagation of medium-scale atmospheric gravity waves at mid-latitudes. *Journal of Atmospheric and Terrestrial Physics*, 46(3), 217–231. [https://doi.org/10.1016/0021-9169\(84\)90149-1](https://doi.org/10.1016/0021-9169(84)90149-1)
- Waldock, J., & Jones, T. (1986). HF Doppler observations of medium-scale travelling ionospheric disturbances at mid-latitudes. *Journal of Atmospheric and Terrestrial Physics*, 48(3), 245–260. [https://doi.org/10.1016/0021-9169\(86\)90099-1](https://doi.org/10.1016/0021-9169(86)90099-1)
- Waldock, J., & Jones, T. (1987). Source regions of medium scale travelling ionospheric disturbances observed at mid-latitudes. *Journal of Atmospheric and Terrestrial Physics*, 49(2), 105–114. [https://doi.org/10.1016/0021-9169\(87\)90044-4](https://doi.org/10.1016/0021-9169(87)90044-4)
- Yigit, E., & Medvedev, A. S. (2015). Internal wave coupling processes in Earth's atmosphere. *Advances in Space Research*, 55(4), 983–1003. <https://doi.org/10.1016/j.asr.2014.11.020>
- Yigit, E., & Medvedev, A. S. (2017). Influence of parameterized small-scale gravity waves on the migrating diurnal tide in Earth's thermosphere. *Journal of Geophysical Research: Space Physics*, 122, 4846–4864. <https://doi.org/10.1002/2017JA024089>
- Zhang, S. D., & Yi, F. (2002). A numerical study of propagation characteristics of gravity wave packets propagating in a dissipative atmosphere. *Journal of Geophysical Research*, 107(D14), 4222. <https://doi.org/10.1029/2001JD000864>